Title	Effect of magnetism on lattice dynamics in Sr(Fe1-xCox)2As2 as seen via high-resolution inelastic x-ray scattering
Author(s)	村井, 直樹
Citation	大阪大学, 2016, 博士論文
Version Type	VoR
URL	https://doi.org/10.18910/56091
rights	
Note	

Osaka University

Department of Physics,

GraduateSchool of Science

Effect of magnetism on lattice dynamics in $\mathbf{Sr(Fe_{1-x}Co_x)_2As_2}$ as seen via high-resolution inelastic x-ray scattering

Naoki Murai

Abstract

This thesis explores the lattice dynamics of iron-pnictide high-temperature superconductors using high-resolution inelastic x-ray scattering (IXS). Current understanding of iron-pnictide superconductors generally does not favor phonon-mediated pairing, but there remain several puzzles regarding the phonon behavior, including (1) an experimental failure to observe expected phonon splittings in the magnetically ordered state at finite momentum transfers, (2) a general failure of calculations to agree with phonon behavior. The present work uses uniaxial pressure to detwin single crystals of $Sr(Fe_{1-x}Co_x)_2As_2$, allowing observation of mode splitting in the magnetically ordered phase. The result is used in combination with *ab-initio* calculations to construct a model of phonon behavior that provides a good fit to the experimental data for both the antiferromagnetically ordered phase and the paramagnetic phase. In analogy to the small ordered moment in iron-pnictides, we suggest that the presence of magnetic fluctuations significantly reduces the phonon anisotropy that reflects the coupling to the static magnetic order. The implications of these results will be discussed in relation to the the underlying magnetic state of iron-pnictides.

Acknowledgements

Contents

List of Tables

List of Figures

Chapter 1

High-Temperature Superconductivity in Iron-Based Materials

1.1   Introduction

Superconductivity is among the most fascinating phenomena in condensed matter. On the fundamental level, it is a remarkable macroscopic manifestation of quantum mechanics. The Bardeen-Cooper-Schrieffer (BCS) theory developed in the late 1950s [1] provided a conceptual framework within which to understand conventional superconductivity. Fundamental to the BCS theory of superconductivity is the fact that the electrons can collectively bind into so-called Cooper pairs and simultaneously condense into a superfluid state by exchanging phonons. For phonon-mediated BCS superconductors, it was widely believed that the superconducting transition temperature T_c cannot

exceed 30 K (with the exception of metallic hydrogen [1])[3]. In fact, during 1970s, the highest T_c had been stuck at 23 K of Nb_3Ge [4], which provided proof of the BCS T_c limit of 30 K.

However, following the long stagnation in the search for highter T_c materials, two major breakthroughs occurred in the history of superconductivity. The first was the discovery in 1986[5] of the layered copper oxides (cuprates). Within a few years, the T_c's of these compounds greatly exceeded those of any previously known superconductors by roughly an order of magnitude (see Fig. 1.1). The maximum T_c reached at ∼ 130 K[6] (∼ 160 K under high pressure[7]) in the mercury-based cuprate. The unusually high-T_c
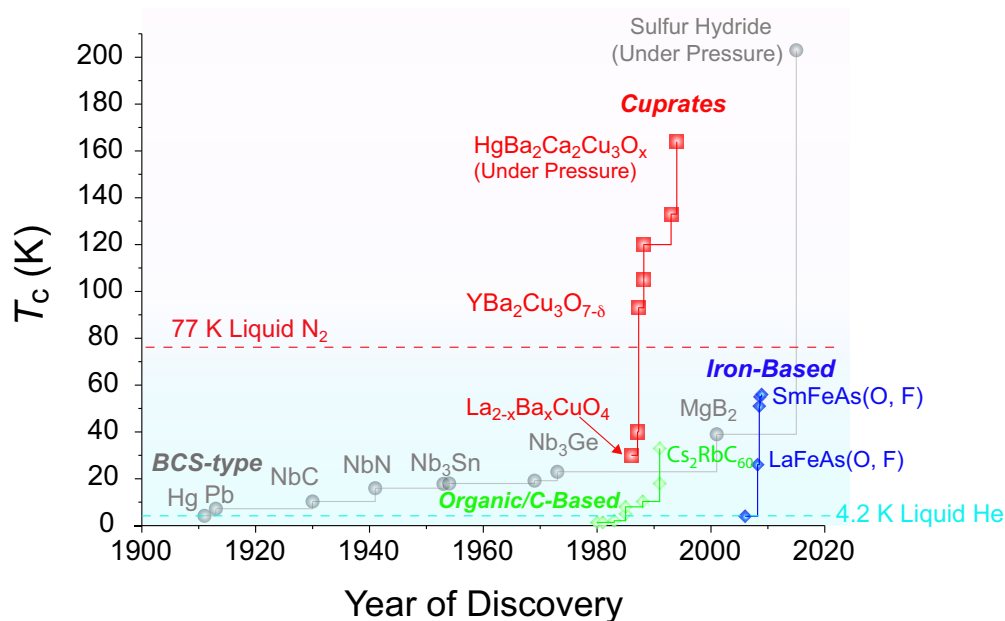
Figure 1.1: Superconducting transition temperatures T_c versus year of discovery for various classes of superconductors.

---

[1]The metallization of hydrogen has long been a challenging problem in high-pressure research, because it is believed to be a route for achieving high-T_c superconductivity. It is only now that this idea has been demonstrated by the discovery of high-T_c superconductivity in high-pressure hydrogen sulfide system at about 200 K[2], where superconducting phase is induced by the conventional mechanism due to high-frequency hydrogen phonon modes.

in the cuprates together with unusual normal state properties, which cannot be described within the framework of the Fermi liquid picture[8], place the cuprates in the broad category of unconventional superconductor. Interestingly, the BCS theory of superconductivity is inapplicable to unconventional superconductors where electron-electron interaction plays an important role in electron pairing rather than electron-phonon interaction. Therefore, whenever a new superconductor is found, one of the first questions to be asked is whether it is conventional or unconventional.

The second breakthrough was the discovery in 2008[9] of layered iron-based superconductors with T_c's up to 55 K[10]. Their discovery demonstrated that unconventional high-T_c superconductivity, such as that found in the cuprates 29 years ago, is not a unique phenomenon but is probably as ubiquitous as the conventional low-T_c superconductors. More importantly, in both families, superconductivity emerges in close proximity to an antiferromagnetic phase. This led to the conjecture that magnetic fluctuations are involved in the pairing mechanism that leads to the high-T_c superconductivity. Therefore, iron-based superconductors could provide a new testing ground for microscopic theories of unconventional superconductors because they share many common physical properties with cuprates. The aim of this chapter is to provide an overall picture of the iron-based superconductors, highlighting the basic physical properties and the underlying physics of iron-pnictide superconductors.

1.2 Material Variation and crystal structures

The crystal structures of iron-pnictide family share a common layered structure consisting of a square lattice of iron atoms with tetrahedrally-coordinated

pnictogen anions that are either simply stacked together, as in FeSe, or are separated by blocking layers. These common structural features found in iron-pnictide materials are similar to the common copper-oxygen building block in the cuprate superconductors. However, one should note the important difference regarding the arrangement of the pnictogen ions which are located above and below the planar iron layer (see Fig. 1.2 (b)), as opposed to the planar copper-oxygen structure of the cuprates. The crystal structures of four typical
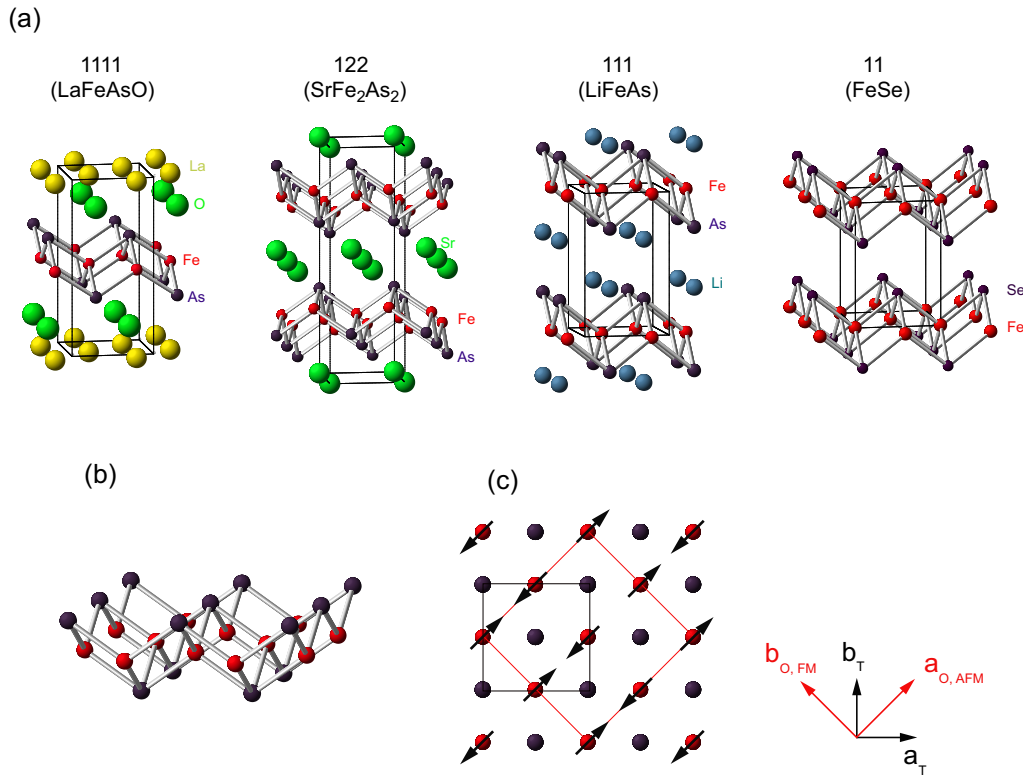
Figure 1.2: (a) The schematic view of the crystal structures for several types of iron-based superconductors. (b) The common structural feature of iron-based superconductors is the presence of FeAs plane (FeSe plane in the case of 11 systems), with iron ions shown in red and pnictogen/chalcogen anions in blue, respectively. (c) The collinear AFM structure in the FeAs plane, where the black box indicates the tetragonal crystalline unit cell in the paramagnetic state, while the other red box indicates the orthorhombic magnetic unit cell. The a_T and b_T correspond to directions of the tetragonal lattice, while the $a_{O, AFM}$ and $b_{O, FM}$ correspond to the orthorhombic lattice.

Materials	$a_{\mathrm{T}}(\text{Å})$	$c(\text{Å})$	$T_s(\text{K})$	$T_{\mathrm{N}}(\text{K})$	moment/Fe (μ_{B})
LaFeAsO[22, 23]	4.0301	8.7368	155	137	0.36
CeFeAsO[24]	3.9959	8.6522	158	140	0.80
PrFeAsO[25]	3.997	8.6057	153	127	0.48
NdFeAsO[26, 27]	3.9611	8.5724	150	141	0.25
CaFe$_2$As$_2$[28, 29, 30]	3.912	11.667	173	173	0.80
SrFe$_2$As$_2$[31, 32, 33]	3.920	12.40	220	220	0.94
BaFe$_2$As$_2$[34, 35]	33.957	12.968	140	140	0.87
NaFeAs[36]	3.9448	6.9968	49	39	0.09

Table 1.1: Summary of the lattice constants in the paramagnetic tetragonal phase, structure transition temperatures T_s, the AFM transition temperatures T_N, and the ordered magnetic moment for parent compounds of the iron-based superconductors.

iron-pnictide family are shown in Fig. 1.2 (a).

The first one is the rare-earth iron-pnictides RFeAsO (R rare earth, the 1111 system) with the ZrCuSiAs-type tetragonal structure (space group $P4/nmm$). Soon after the first demonstration of high-T_c superconductivity in LaFeAsO$_{1-x}$F$_x$ by Kamihara *et al.*, [9] the optimal T_c increased rapidly up to $\sim 50K$ [10, 11, 12] via replacing lanthanum with other rare-earth elements.

The second class possesses the ThCr$_2$Si$_2$-type body-centered tetragonal structure (space group $I4/mmm$) with the chemical formula AFe$_2$As$_2$ (A = Ba, Sr, Ca, the 122 system). Superconductivity in the 122 system can be induced by ionic substitution at any element site. These include the substitution of Ba with K/Na to form hole-doped Ba$_{1-x}$K$_x$Fe$_2$As$_2$ [13, 14, 15], Fe with Co or Ni to form electron-doped BaFe$_{2-x}$T$_x$As$_2$(T = Co, Ni) [16, 17, 18] and As with P in the isovalent-doped BaFe$_2$(As$_{1-x}$P$_x$) [19, 20, 21].

The third system is AFeAs (A = Li, Na, the 111 system) with the tetragonal PbFCl-type structure (space group $P4/nmm$). Unlike the 1111- and the 122-type iron-pnictide superconductors, LiFeAs exhibits superconductivity with T_c of 18 K without chemical substitution[37, 38].

The last one is the tetragonal PbO-type FeSe (the 11 system), which has the simplest crystallographic structure among the iron-based superconductors. Although the T_c of FeSe is as low as ~ 8 K [39, 40, 41], the onset of superconductivity rises to 15 K with partial substitution of Te for Se[42, 43], or to 37 K under high pressure[44].

The crystal structures of parent iron-pnictide superconductors at room temperature are all tetragonal, and some of them exhibit a tetragonal to orthorhombic structural transition at low temperatures below T_s that either precedes or is coincident with the long-range antiferromagnetic (AFM) spin-density-wave (SDW) ordering below T_N with moment aligned along the $a_{\mathrm{o,AFM}}$ axis of the orthorhombic lattice (see Fig. 1.2 (c)). Much of this behavior can be understood in terms of density functional theory (DFT) calculations. Although such calculations have a tendency to yield larger Fe moment than is observed experimentally[45, 46], they suggest that the stripe-type AFM structure is the only stable ground state, and that this structure is stabilized by the orthorhombic structural deformation[47]. In Table1.1, the lattice parameters, structure transition temperature T_s, the AFM transition temperature T_N and the static ordered moments per iron for the parent compounds of iron-based superconductors are summarized.

1.3 Phase diagram and tuning parameters

The phase diagram of the iron-pnictide superconductors is remarkably similar to that of other classes of unconventional superconductors, including the copper oxides and heavy fermions, in which the pairing interaction respon-
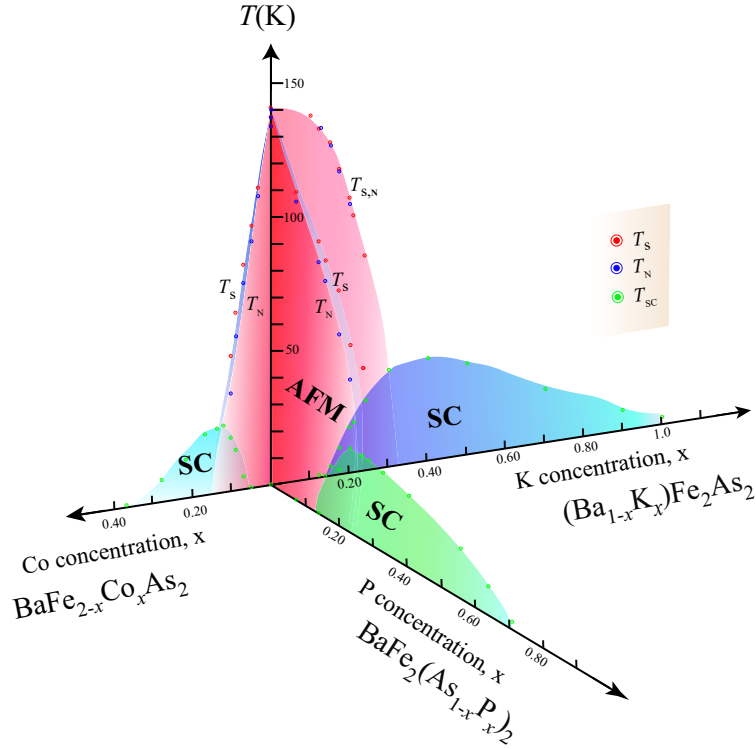
Figure 1.3: Schematic phase diagram of BaFe$_2$As$_2$. Experimental data on the transition temperatures were taken from Ref[13] for hole-doped (Ba$_{1-x}$K$_x$)Fe$_2$As$_2$, Ref[48] for electron-doped BaFe$_{2-x}$Co$_x$As$_2$ and Ref[21] for isovalent doped BaFe$_2$(As$_{1-x}$P$_x$)$_2$.

sible for superconductivity may be mediated by spin fluctuations. The general phase diagram of iron-pnictide systems can be produced either by chemical substitution or applied external pressure to drive an AFM parent compound to a superconducting (SC) state. A complicated phase diagram is schematically presented in Fig.1.3 for the BaFe$_2$As$_2$ system, which is so far the most studied due to the availability of high-quality single crystals, and thought to capture the main features of iron-pnictide compounds. In Ba-122 system, the systematic substitution of either the alkaline-earth (Ba), transition-metal (Fe) or pnictogen (As) site with a different element universally produces the phase diagram composed of the three phase transitions, i.e., the supercon-

ducting, antiferromagnetic, and structural ones. From this figure one can see the quantitative similarity between phase diagrams produced by chemical substitutions involving hole doping in $Ba_{1-x}K_xFe_2As_2$ [13, 14] and electron-doping in $BaFe_{2-x}Co_xAs_2$ [16, 17], as well as nominally isovalent-doping in $BaFe_2(As_{1-x}P_x)$ [19, 20, 21]. This highlights the idea that simple charge doping, as in the cuprates, is not the sole factor that determines the phase boundaries of iron-based materials, and that structural tuning can also play a key role.

Another important feature to be mentioned here is that AFM order coexists with superconductivity in the underdoped regime [49, 50, 51]. Neutron diffraction showed a reduction of the static Fe moment in coexistence phases of $BaFe_{2-x}Co_xAs_2$ on entering the SC state[50], providing strong evidence that AFM order and superconductivity coexist, and interestingly, may be in competition with each other. Such a coexistence phase has also been observed in the 1111 system $SmFeAsO_{1-x}F_x$[52]. [2]

1.4 Electronic structure

Iron-pnictide superconductors share some similarities with the cuprate superconductors, such as a layered structure and close proximity of the AFM order and superconductivity in their respective phase diagrams. However, there are important differences between the two systems. In particular, these differences arise mainly from the multi-orbital nature of the electronic structure in iron-pnictides.

In the cuprates, the low-energy physics is governed by Cu $3d_{x^2-y^2}$ and

---

[2]We note that, in contrast to $SmFeAsO_{1-x}F_x$[52], the other 1111 system including $LaFeAsO_{1-x}F_x$[53] and $CeFeAsO_{1-x}F_x$[54] do not show a coexistence of AFM order and superconductivity[53].

O 2p orbitals, allowing the reduction of the multi-band electronic structure to an effective one-band model[55]. In iron-pnictides, on the other hand, the minimal model is essentially multiband, which makes physical properties of these materials more complicated than that of the cuprates. The electronic band structure of iron-pnictides has been calculated on the basis of DFT calculations[56, 57, 58], showing that the electronic properties are dominated by five Fe d-electron orbitals at the Fermi level E_{F}, with small disconnected hole and electron Fermi surfaces. As an example, three-dimensional (3D) Fermi surface for LaFeAsO is shown in Fig. 1.4, where the electronic structure is visualized as several distinct Fermi surface sheets, each corresponding to a different band that crosses E_{F}. Although details vary from one compound to the other, [3] the basic structure of the Fermi surface is similar in all the iron-
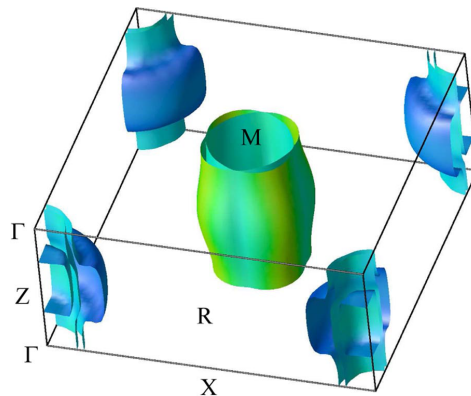
Figure 1.4: Fermi surface of LaFeAsO shaded by velocity [blue is low velocity.] The symmetry points are: $\Gamma = (0,0,0), Z = (0,0,1/2), X = (1/2,0,0), R = (1/2,0,1/2)$ $M = (1/2,1/2,0)$ and $A = (1/2,1/2,1/2)$. Two hole cylinders are at Γ point (corners in the Brillouin zone), an additional heavy 3D hole pocket is centered at Z, and two electron Fermi pockets are at M point. Reprinted with permission from Ref[56]. Copyright (2008) by the American Physical Society.

---

[3]The Fermi surfaces of $BaFe_2As_2$ are similar to those in LaFeAsO, but the hole Fermi surface at the Z point exhibits more three-dimensional character than that in the 1111 and 111 structures. [For example, see Ref.[57, 59] for $BaFe_2As_2$ and Refs.[57] for LiFeAs]

pnictide materials: it consists of electron cylinders centered at the zone corner and hole sections around the zone center. As an important feature of the Fermi surfaces, one should note that the cylinders at the Γ and M points are nearly nested. This suggests the existence of a peak in the spin susceptibility at wave vector $Q = (\pi, \pi)$ in the folded Brillouin zone (two Fe atoms in the unit cell), which results in a spin-density wave (SDW) order with a collinear spin structure, much like the Fermi surface nesting induced SDW state in chromium metal. Indeed, stripe-type SDW state appears as the ground state for the parent compounds of iron-pnictides as confirmed by neutron diffraction [22, 23, 24, 25, 26, 27, 28, 32, 33, 34], thus providing strong evidence for the itinerant origin of the magnetism. This is fundamentally different from the cuprate superconductors, whose parent compounds are AFM Mott insulators due to the strong Coulomb interaction among the electrons. The predicted Fermi surface has been confirmed by angle-resolved photoemission spectroscopy (ARPES) [60, 61, 62, 63, 64], and quantum oscillation[65, 66]. Both measurements find relatively moderate electron correlation, consistent with itinerant behavior of the electrons.

1.5 Superconducting gap structure and symmetry

The superconducting gap structure of the 122 family of iron-pnictides has been extensively studied by ARPES due to the availability of high-quality single crystals. Fig. 1.5 summarizes the results of ARPES measurements on the superconducting $Ba_{0.6}K_{0.4}Fe_2As_2$ with T_c of 37 K[60]. Although the magnitude of the superconducting gap differs in size from one Fermi surface to the
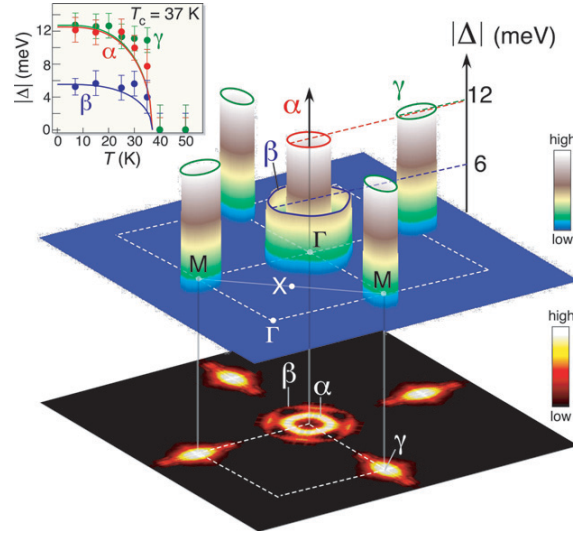
Figure 1.5: The Fermi surface and superconducting gap of $Ba_{0.6}K_{0.4}Fe_2As_2$ as determined from ARPES. (Reprinted from Ref[60].) The three-dimensional plot shows the gap measured at 15 K on the three Fermi surface sheets, with the color indicating the gap size.

other, the gap anisotropy on each Fermi surface is relatively weak, suggesting the *s*-wave symmetry. Fully gapped superconductivity has also been suggested in the optimally doped regime of electron-doped $BaFe_{2-x}Co_xAs_2$[67].

Based on these measurements showing a relatively isotropic gap, one might argue that superconductivity in iron-pnictides is of conventional nature, where the electron-pairing is phonon mediated. However, DFT calculations suggested that the electron-phonon coupling is too weak to account for the observed high-T_c, implying that the superconductivity is not phonon mediated[68]. In fact, a growing body of theoretical work suggests the possibility of spin fluctuation mediated unconventional superconductivity arising from nesting between disconnected Fermi surfaces [69, 70]. If such a spin fluctuation is responsible for the electron-pairing in iron-based superconductors, a sign reversal of the the gap function is expected between the hole and the electron pockets, leading to the so-called isotropic $s_\pm$ state[69, 70]. Experimentally, the

sign reversal of the gap function has indeed been suggested for $Fe(Te, Se)$ by the quasi-particle interference pattern of scanning tunneling microscopy[71].

1.6 Electronic nematicity

In many materials, anisotropic properties are related to the point-group symmetry of the underlying crystal lattice. However, electron-electron correlations may also lead to anisotropic electronic state which spontaneously breaks the orientational symmetry of the underlying lattice[72]. This is often referred to as "nematicity" in analogy to liquid-crystal. Recently, evidence of nematicity has been observed in close proximity to the superconducting phase of the cuprate superconductors [73, 74, 75]. Similarly, the iron-pnictide superconductors also exhibit a nematic phase in the form of a tetragonal ($I4/mmm$) to orthorhombic ($Fmmm$) structural phase transition below T_s followed by a magnetic phase transition into a collinear AFM ordered phase below $T_N (\leq T_s)$, both of which break the $90°$ rotational C_4 symmetry of the underlying tetragonal lattice. The structural transition and its relation to the AFM order are of great interest, and have been the subjects of intense study. At first glance, one might view this structural distortion as a regular structural transition driven by lattice instability (i.e. phonon). However, some theoretical works suggested that the tetragonal-to-orthorhombic transition is driven by an electronic instability due to orbital ordering of the iron $3d$ electrons which triggers stripe type AFM order[76, 77], or spin-nematic order which induces both structural and orbital order [78, 79]. (For a recent review, see ref.[80].) In both scenarios, a pronounced anisotropy compared to the underlying lattice is a hallmark of electronic nematic phase.
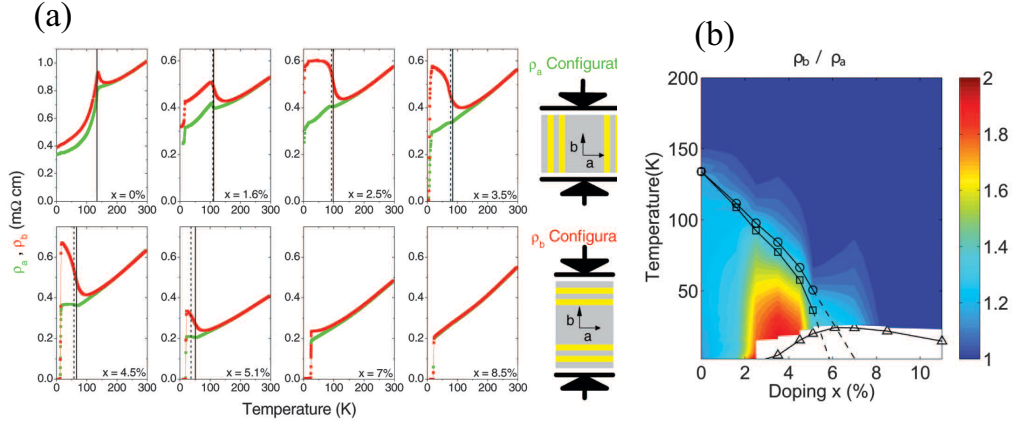
Figure 1.6: In-plane resistivity anisotropy in underdoped iron-based materials. (Reprinted from Ref[16] with permission from AAAS.) (a) Temperature dependence of the in-plane resistivity for $Ba(Fe_{1-x}Co_x)_2As_2$. Solid and dashed vertical lines mark the structural and magnetic phase transitions T_s and T_N, respectively. (b)Temperature and composition dependence of the in-plane resistivity anisotropy ρ_b/ρ_a for $Ba(Fe_{1-x}Co_x)_2As_2$. Structural, magnetic and superconducting critical temperatures are shown as circles, squares, and triangles, respectively.

The first experimental support for the electronically-driven tetragonal-to-orthorhombic transition comes from measurements of the resistivity anisotropy of the detwinned crystal of $Ba(Fe_{1-x}Co_x)_2As_2$, with the resistivity along the shorter b axis ρ_b being greater than that along the longer a axis ρ_a[16] (see Fig.1.6 (a)). The observed in-plane resistivity anisotropy is anomalously large given the small in-plane distortion between the a- and b-axis lattice parameters in the orthorhombic phase $((a - b)/(a + b) \leq 0.36\%)$. Notably, the resistivity anisotropy is evident for temperature range well above T_s even though the crystal symmetry is tetragonal (see Fig.1.6 (b)). This suggests the presence of nematic fluctuations above T_s that breaks the rotational C_4 symmetry of the underlying lattice [4].

---

[4]Note that recent transport measurement[81] suggests that the resistivity anisotropy arises from impurity scattering, and therefore is not an intrinsic property of iron-pnictide materials.

In addition to dc resistivity, the optical conductivity of the detwinned $BaFe_2As_2$ was also found to exhibit a pronounced anisotropy, persisting up to an unexpectedly high energy of about 2 eV[82]. ARPES [83, 84, 85] and quantum oscillation[65] studies further revealed an in-plane electronic anisotropy with C_2 rotational symmetry. Intriguingly, some ARPES studies reported an energy splitting between the d_{xz} and d_{yz} orbitals that occurs well above T_s corresponding to the onset of the in-plane resistivity anisotropy, thus suggesting the involvement of the orbital order in the nematic phase[83, 84].

Anisotropies related to the nematic order were also found in the spin channel. Inelastic neutron scattering (INS) study showed that low-energy spin excitations of $Ba(Fe_{1-x}Ni_x)_2As_2$ change from C_4 symmetry to C_2 symmetry at temperature range above T_s where the resistivity anisotropy is observed. Further, magnetic torque magnetometry revealed the breaking of the C_4 rotational symmetry in a tetragonal crystal structure well above T_s[86]. Interestingly, the observed onset of magnetic anisotropy coincides with that of orthorhombic distortion, consistent with the idea of electronically-driven tetragonal-to-orthorhombic transition.

The experimental evidence described above supports the idea that nematic order in iron-pnictide materials is of electronic origin. Although disentangling the orbital and magnetic scenarios is difficult and still controversial at least on an experimental level, in any case, all three orders (e.g., structural, orbital, and magnetic) appear in the nematic phase, which provides a unique opportunity for studying spin-orbital-lattice coupled phenomena in strongly correlated electron systems.

Chapter 2

Context and Purpose of this thesis

The close proximity of superconductivity to an AFM phase in the iron-pnictides suggests that magnetic fluctuations are involved in the pairing mechanism that leads to the high-T_c superconductivity. In fact, in early work, DFT calculations suggested that the electron-phonon coupling is too weak to account for the observed high-T_c[68], implying that the superconductivity is not phonon mediated.

On the other hand, the physical properties of iron-pnictides do exhibit a strong sensitivity to the lattice. One important and interesting feature is the relation between crystal structure and superconductivity. For example, Lee *et al*. parametrized the T_c in terms of As-Fe-As bond angle α for various iron-pnictide materials, showing that T_c seems to be maximized at $\alpha \sim 109°$ at which FeAs$_4$-lattices form a regular tetrahedron[87]. [1] Anion height h from the Fe layer has also been suggested as an alternative factor affecting T_c[88]. This work was motivated by a theoretical study by Kuroki *et al*. that proposes

---

[1]The importance of the bond angle has also been suggested in Ref[54].

the value of h as a possible switch between high-T_c nodeless and low-T_c nodal pairings in iron-pnictide materials[89].

One should also note that there is a strong coupling of the magnetic degrees of freedom to the lattice. Probably the most striking indication of such a coupling is the well-known collapsed tetragonal structure of $CaFe_2As_2$, where the c-axis contracts by about 10 % with the loss of Fe-magnetism[47]. The response of lattice to the change of magnetism is called magneto-elastic coupling, and usually its magnitude is tiny and hardly measurable by neutron or x-ray scattering. However, this effect is huge for the case of iron-pnictide materials[90], which motivates us to investigate the magneto-elastic coupling of these materials from the viewpoint of phonon spectroscopy.

The phonon spectrum and its temperature dependence have been extensively studied by inelastic x-ray scattering (IXS) and inelastic neutron scattering (INS) for various iron-pnictides compounds including 1111 system [$LaFeAsO_{1-x}F_x$[91, 92, 93, 94], $PrFeAsO_{1-x}$[91, 95] $NdFeAsO_{1-x}F_x$[93], and $SmFeAsO_{1-x}F_x$[96]], 122 system [$(Ba_{1-x}K_x)(Fe_{1-y}Co_y)_2As_2$[97, 98, 99, 100, 101], $SrFe_2As_2$[102], and $CaFe_2As_2$[103, 104]] and 11 system [$FeSe_{1-x}$[105]]. Although these studies did not find any significant changes in the observed phonon response with superconductivity, some of them indicate disagreement with non-magnetic DFT calculations. For example, Fukuda et $al.$ found that the room-temperature phonon density of states (DOS) in LaFeAsO cannot be explained unless the calculated Fe-As force constants are reduced by 30 %[91]. Subsequent studies have shown that the inclusion of magnetism in the calculations reduces the energy of some modes to be closer to the experimental data[94, 95, 97, 104]. Interestingly, phonon frequencies were unaffected by the suppression of the static long-range magnetic order either by
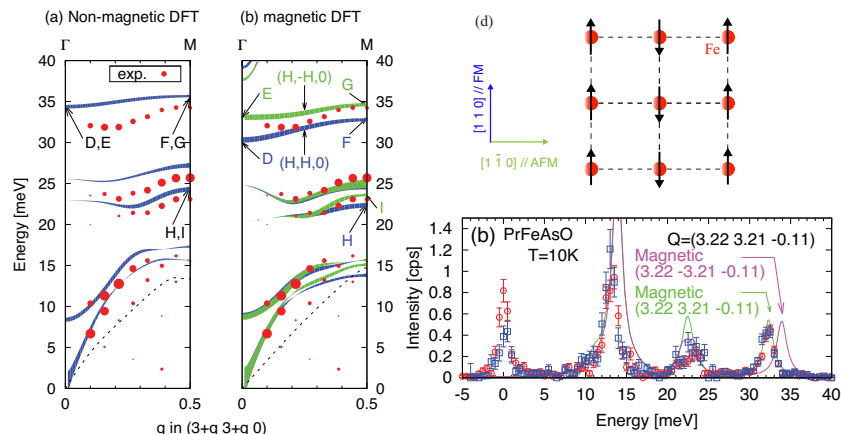
Figure 2.1: Comparison of the measured dispersion for $PrFeAsO_{1-x}$ and DFT calculations at $\mathbf{Q} = (3 + q, \pm(3 + q), 0)$ [95]. The non-magnetic DFT calculation in (a) clearly overestimates the energy of the highest optical mode at ~ 35 meV. The magnetic DFT calculation in (b) dramatically improves agreement with the data, but also predicts large splitting of the mode at $\sim 30 - 35$ meV that is not observed in the experiment. (c) Phonon spectra at $\boldsymbol{Q} = (3.22, \pm 3.21, -0.11)$. The points correspond to the experimental data, while the lines correspond to the magnetic DFT calculations of the phonon structure factor convoluted with the instrumental resolution. (d) The AFM spin arrangement of iron in the Fe-As layer. Note that mode splitting in magnetic DFT occurs because calculated frequencies of phonons with wave vectors along [110] direction depend on the spin orientation relative to the phonon wave vector. Reprinted with permission from Ref[95]. Copyright (2011) by the American Physical Society.

doping or increased temperature [95, 97]. This might support the view that the Fe magnetic moment should be present in iron-pnictides at all times in the form of fluctuating SDW type small magnetic domains as suggested by Mazin and Johannes[46]. However, magnetic DFT calculations predict a pronounced phonon anisotropy characterized by splitting of phonon modes that is not observed in the experiment[95, 97]. Despite the growing number of evidence of anisotropic behaviour in iron-pnictides as discussed in Sec.1.6, the phonon response is surprisingly isotropic. Phonon anisotropy should exist, in principle, and mode splitting has been seen using Raman scattering[106], but anisotropy

has not been observed at non-zero momentum transfers.

Thus, while current understanding of iron-pnictide superconductors generally does not favor phonon-mediated pairing, there remain outstanding puzzles regarding the phonon behavior in these materials as summarized below:

- While no anomalous phonon modes, as found in the cuprates [107, 108, 109], have been observed in iron-pnictides, there is a general failure of non-magnetic DFT calculations to predict phonon energies in either the AFM or the paramagnetic (PM) phases.

- Inclusion of magnetism brings the calculation into better agreement with the experimental data, but also predicts large splitting of phonon modes that is not observed in the experiment.

These issues are exemplified in Fig.2.1[95], where non-magnetic DFT calculation does not agree with the experiment (see Fig.2.1 (a)), while magnetic DFT calculation predicts a large mode splitting that is not observed in the experiment (see Figs.2.1 (b) and (c))

To gain insight into this problem, we performed meV-resolved IXS at SPring-8 on single crystals of $Sr(Fe_{1-x}Co_x)_2As_2$. Since the interesting phonon modes are Fe and As vibrations, both of which are relatively heavy materials, IXS is the method of choice for investigating phonons in iron-pnictides. The present work uses uniaxial pressure to detwin single crystal, allowing observation of mode splitting in the AFM ordered phase. The result is used in combination with DFT calculations to construct a model of phonon behavior that provides a good fit to the experimental data for both the AFM ordered phase and the PM phase. Based on this analysis, the underlying magnetic state of iron-pnictides and its effect on lattice dynamics are discussed.

Chapter 3

Experimental Details

3.1 Phonon spectroscopy using inelastic x-ray scattering

[1]

3.1.1 Introduction

Since its discovery, x-ray diffraction has been an established tool for investigations of the local arrangement of atoms and molecules in condensed matter. In the early days of x-ray diffraction, the diffraction spots only gave information on the static order in the atoms. It was soon demonstrated that the thermal movements of the atoms in a crystal are responsible for an attenuation of the intensities of the Bragg peaks by Debye-Waller factor, and therefore the diffuse scattering intensities between the diffraction spots contain information on the lattice dynamics. In fact, historically, phonon dispersions were

---

[1]Discussion in this section draws heavily from Refs[110, 111] where further details can be found.

first determined from thermal diffuse scattering (TDS) in combination with the theory of lattice dynamics.[112].

However, energy-resolved measurements of TDS faced a formidable experimental challenges, mainly due to the required extremely high energy resolution. This can be understood by considering that x-rays with wavelength comparable to interatomic scale have energies of about ~ 10 keV. Therefore, resolving the $\sim$ meV phonon excitations requires energy resolution of at least $\Delta E/E = 10^{-7}$. At that time, only thermal neutrons allowed direct measurements of the whole phonon dispersion relations, making inelastic neutron scattering (INS) the leading method in phonon spectroscopy as a momentum and energy resolved technique[113].

However, the situation changed with the advent of synchrotron radiation sources. The first pioneering work in IXS was demonstrated at HASYLAB at DESY in Hamburg, Germany [114] in 1980s. Since then, with the advent of third-generation synchrotron radiation sources, and the success of the first IXS beamline at the European Synchrotron Radiation Facility (ESRF)[115] in the middle of 1990s, IXS has matured into a valuable spectroscopic technique that is complementary to INS. Nowadays, thanks to the extremely high brilliance of the undulator sources and development of x-ray optics with very high energy resolution, IXS experiments can be performed with an energy resolution of 1.5 meV. There are now five worldwide facilities dedicated to IXS with resolution between 1 and 6 meV, including one beamline, ID28 at the European Synchrotron Radiation Facility (ESRF) in Grenoble France, two beamlines, sector 3 and sector 30 at the Advanced Photon Source (APS) in Argonne, Illinois in the US, and two beamlines, BL35XU and BL43LXU of SPring-8 in Harima Science Garden City of Hyogo Prefecture, Japan.

3.1.2 Comparison of IXS with INS for phonon measurements

Since the study of lattice excitations, phonons, has long been the domain of inelastic neutron scattering (INS), it is worthwhile to compare IXS and INS. More detailed discussion and comparison of these two methods as well as alternative techniques can be found in Ref[110, 111]. The most fundamental difference between IXS and INS is that IXS probes the coherent motion of the electrons while INS probes the nuclear motion. The equivalence of the two methods can be verified within the limits of the adiabatic approximation, where the electrons instantaneously follow the motions of the nuclei. It means that phonons (i.e. motions of the nuclei), will cause the variations of electron charge density, which can then be directly probed by x-rays. There are other differences between the two methods, and some of the characteristics of IXS as compared to INS are listed as follows:

1. Availability of small, ($\sim \mu$g) samples.

2. Decoupling of energy and momentum transfer.

3. Energy resolution that is independent of the energy transfer.

4. Nearly no intrinsic background.

The ability of IXS to probe small samples, (1) above, is probably the most advantageous aspect of IXS. This has been made possible by the high flux and high brilliance of synchrotron radiation sources, with beam size down

to few tens of μm, allowing one to investigate small samples which are inaccessible by the traditional methods of INS, including the cases where large single crystals are generally not available[116, 117, 118], and experiments are performed under extreme conditions using diamond anvil cells (DACs) [119].

The second and third characteristics of IXS are directly the result of the fact that incident energies of x-rays are much larger than the measured energy transfers, in contrast with neutrons where the probe energy is comparable to the phonon energy scales, and therefore, kinematic constraints are no longer relevant in IXS. Consequently, IXS offers the unique opportunity to measure practically unlimited energy transfer in the accessible momentum transfer range of $\sim 1 - 100$ nm^{-1}. This is especially important for the study of the high-frequency dynamics of liquids and glasses[115, 120, 121] where one would like access to large energy transfer at small momentum transfers.

IXS also differs from INS in that there are few sources of background. This is related with the fact that (1): x-ray penetration depths in most materials are so short as to prevent multiple scattering, and that (2): incoherent (Compton) scattering with x-rays occurs at larger energy transfer $> eV$ due to the small electron mass. Therefore, the multiphonon contribution is the only intrinsic background for IXS work at phonon energy scales[117].

INS remains advantageous when high-energy resolution is needed, as has been demonstrated by backscattering spectrometer [122, 123] and spin echo spectrometer[124] that provide μeV level, or even better, energy resolution. In fact, the precise determination of the lifetimes of acoustic phonons with μeV energy resolution is made possible by recent advances in spin-echo spectroscopy[125].

3.1.3   Scattering theory and phonon cross section

In this section, we outline the scattering cross section and the dynamic structure factor $S(\boldsymbol{Q}, \omega)$. A more detailed treatment of this subject is given in Refs.[110, 111, 126, 127, 128]

The results of a scattering experiment are usually compared with theory in terms of the scattering cross section. The basic kinematics of a typical inelastic scattering experiment are schematically illustrated in Fig.3.1. The incident beam of energy $E_1 (= \hbar\omega_1)$, wavevector $\boldsymbol{k}_1$ and polarization vector $\boldsymbol{\epsilon}_1$ is scattered into the solid-angle element $d\Omega$ under the scattering angle 2θ. The scattered beam is defined by the energy $E_2 (= \hbar\omega_2)$, wavevector $\boldsymbol{k}_2$ and the polarization vector $\boldsymbol{\epsilon}_2$. The energy $\hbar\omega = \hbar(\omega_1 - \omega_2)$ and the momentum $\hbar\boldsymbol{Q} = \hbar(\boldsymbol{k}_1 - \boldsymbol{k}_2)$ are transferred to the target. As long as $E << E_1$, the modulus of the transferred momentum is connected with the scattering angle 2θ by

$$\hbar Q = 2k_1 \sin\theta. \tag{3.1}$$

Thus, a typical inelastic scattering experiment consists of (1) producing a
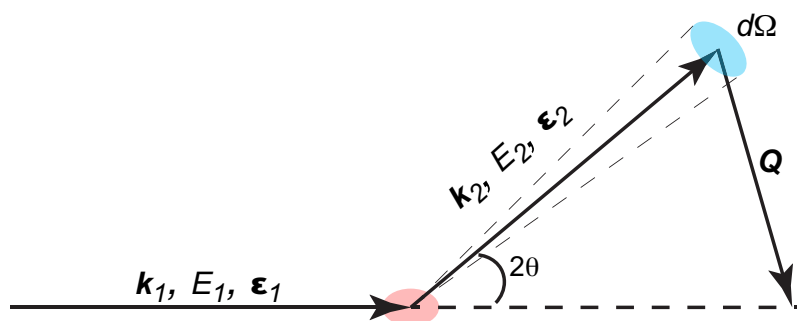
Figure 3.1: Inelastic scattering geometry. $E_{1(2)}$, $\boldsymbol{k}_{1(2)}$ and $\boldsymbol{\epsilon}_{1(2)}$ are the energy, wavevector and polarization vector of the incident (scattered) beam. 2θ is the scattering angle and $\boldsymbol{Q}$ is the momentum transfer due to the scattering process.

well-collimated beam, (2) selecting a certain solid angle $d\Omega$ of the scattered beam, so that $\boldsymbol{Q}$ is fixed according to Eq.3.1, and (3) energy-analyzing this part of the scattered radiation to a resolution of $d\omega$. In other words, the scattered intensity is measured by the double-differential scattering cross section (DDSCS), $d^2\sigma/d\Omega d\omega$ as function of $\boldsymbol{Q}$ and ω.

Within the limits of the first-order perturbation treatment (lowest order Born approximation), the DDSCS is related to the dynamic structure factor, $S(\boldsymbol{Q},\omega)$,

$$\frac{d^2\sigma}{d\Omega d\omega} = \left(\frac{d\sigma}{d\Omega}\right)_o S(\boldsymbol{Q},\omega),\tag{3.2}$$

where $(d^2\sigma/d\Omega)_O$ is the intrinsic cross section related to probe-sample interaction. The proportionality to $S(\boldsymbol{Q},\omega)$ shows that the spectrum of the density fluctuations of the system can be directly obtained by measuring the scattered x-rays as a function of $\boldsymbol{Q}$ and ω.

The coupling of the electromagnetic field of the photon to the electrons of the system ic characterized by the intrinsic cross section $d\sigma/d\Omega_o$, and taken into account in terms of the Thomson scattering cross section of a single electron,

$$\begin{aligned}\left(\frac{d\sigma}{d\Omega}\right)_o &= \left(\frac{d\sigma}{d\Omega}\right)_{\text{Th}}\\ &= r_e^2|\boldsymbol{\epsilon}_1 \cdot \boldsymbol{\epsilon}_2|^2\left(\frac{\omega_2}{\omega_1}\right),\end{aligned}\tag{3.3}$$

where $r_e = 2.818 \times 10^{-15}$ m is the classical electron radius. Since $E << E_1$ as mentioned before, the factor $\left(\omega_2/\omega_1\right)$ in Eq.3.3 is about equal to 1 for non-resonant x-ray scattering. Therefore, $\left(d\sigma/d\Omega\right)_{\text{Th}}$ is of the order of 10^{-30} m^2.

The dynamic structure factor, $S(\boldsymbol{Q},\omega)$, is generally written as the Fourier

transform of the charge density operator,

$$S(\boldsymbol{Q}, \omega) = \frac{1}{2\pi\hbar} \int_{-\infty}^{\infty} dt \ e^{-i\omega t} \langle \rho(\boldsymbol{Q}, 0) \rho(\boldsymbol{Q}^{+}, t) \rangle, \tag{3.4}$$

where we define the charge density operator by

$$\rho(\boldsymbol{Q}, t) = \sum_{i} \rho e^{i\boldsymbol{Q} \cdot r_i(t)}, \tag{3.5}$$

where the sum is over all electron. For crystalline materials, Eq.3.4 is usually simplified by extracting the Debye-Waller factor, and expanding in a power series assuming small atomic displacements as

$$S(\boldsymbol{Q}, \omega) = S(\boldsymbol{Q}, \omega)_{0p} + S(\boldsymbol{Q}, \omega)_{1p} + S(\boldsymbol{Q}, \omega)_{2p} + \cdots, \tag{3.6}$$

where ith term gives the cross section for all ith phonon processes (for details, see Refs.[110, 126]). Thus, the terms of the series in Eq.3.6, correspond to elastic cross section (Bragg reflections), the cross section for all one-phonon processes, and the cross section for all two-phonon processes, respectively. The one-phonon term, $S(\boldsymbol{Q}, \omega)_{1p}$, is generally largest except at Bragg reflections. The explicit form for the one-phonon term for a crystalline material with r atoms in the unit cell can be written [110, 126]

$$S(\boldsymbol{Q}, \omega)_{1p} = N \sum_{\boldsymbol{q}}^{\text{1st Zone}} \sum_{j}^{\text{3r Modes}} F_j(\boldsymbol{Q}) \delta(\boldsymbol{Q} - \boldsymbol{q} - \tau) f_{\boldsymbol{q}j}(\omega), \tag{3.7}$$

$$F_j(\boldsymbol{Q}) = \frac{1}{\omega_{\boldsymbol{q}j}} \left| \sum_{\boldsymbol{d}}^{\text{Atoms/Cell}} f_d(\boldsymbol{Q}) e^{-W_d(\boldsymbol{Q})} \frac{\boldsymbol{Q} \cdot \boldsymbol{e}_{\boldsymbol{q}j\boldsymbol{d}}}{\sqrt{2M_d}} e^{i\boldsymbol{Q} \cdot \boldsymbol{d}} \right|^2,$$

where N is the number of unit cells, $\boldsymbol{Q}$ is the total momentum transfer, $\boldsymbol{q}$ is the reduced momentum transfer in the first Brillouin zone, τ is the nearest Bragg

vector, and j is the index (1 to $3r$) of the phonon mode with energy $\hbar\omega_{qj}$ and the polarization eigenvector $\boldsymbol{e_{qjd}}$. $W_d(\boldsymbol{Q})$, M_d and $f_d(\boldsymbol{Q})$ are Debye-Waller factor, atomic mass and the x-ray atomic form factor for the dth atom in the unit cell located at $\boldsymbol{d}$. $f_{qj}(\omega)$ describes the spectral shape and the temperature dependent intensity of the mode. For the simplest case of harmonic phonons, it is given by[110, 126]

$$f_{\boldsymbol{q}j}(\omega) = \langle n_{\omega_{\boldsymbol{q}j}} + 1 \rangle \delta(\omega - \omega_{\boldsymbol{q}j}) + \langle n_{\omega_{\boldsymbol{q}j}} \rangle \delta(\omega + \omega_{\boldsymbol{q}j}), \tag{3.8}$$

where the thermal occupation function is taken into account through the Bose-Einstein distribution $\langle n_{\omega_{\boldsymbol{q}j}} + 1 \rangle = (1 - e^{-\hbar\omega_{\boldsymbol{q}j}/k_BT})^{-1}$. Note that we take positive energy transfer, $\hbar\omega > 0$, to the higher intensity side of the IXS spectra corresponding to giving energy to the sample or Stokes scattering. The generalization of Eq.3.8 to allow for the finite phonon line-width, as is important for MgB_2[116, 117, 118], is possible using a damped harmonic oscillator (DHO) line shape[129]

$$f_{\boldsymbol{q}j}(\omega) = \frac{1}{\pi} \frac{1}{1 - e^{-\hbar\omega/k_BT}} \frac{4\omega\omega_{\boldsymbol{q}j}\gamma_{\boldsymbol{q}j}}{(\omega^2 - \Omega_{\boldsymbol{q}j}^2)^2 + 4\omega^2\gamma_{\boldsymbol{q}j}^2}, \tag{3.9}$$

where $\gamma_{\boldsymbol{q}j}$ is the phonon line-width (half width at half maximum), and $\Omega_{\boldsymbol{q}j}^2 = \omega_{\boldsymbol{q}j}^2 + \Gamma_{\boldsymbol{q}j}^2$ is the effective frequency of the mode. Note that in the limit of small $\gamma_{\boldsymbol{q}j}$, Eq.3.9 reduces to Eq.3.8.
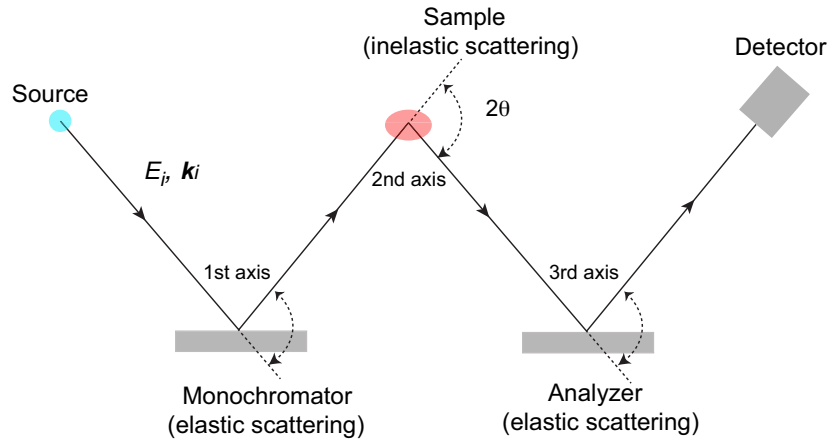
Figure 3.2: Schematic illustration of a triple-axis spectrometer for inelastic scattering.

3.1.4 IXS spectrometers

The triple-axis spectrometer

The modern IXS spectrometer is essentially a conventional 4-circle x-ray diffractometer with an energy-scan option, conceptually rather similar to a triple-axis spectrometer, which was first developed by Brockhouse for inelastic neutron scattering (INS) studies. Triple-axis means that instrument has three axes composed of the high energy resolution monochromator (first axis), the goniometer setup for defining the sample orientation (second axis) and the crystal analyzer (third axis) (see Fig.3.2). The incident energy and wavevector of the probe is well defined in energy E_i and wavevector $\mathbf{k}_i$ by elastic scattering from a monochromator crystal. For x-rays, this is usually done by a Bragg reflection of a silicon or diamond crystal. After the inelastic scattering process at the sample position with a scattering angle of 2θ, the scattered beam is analyzed for energy E_f and wavevector $\mathbf{k}_f$ by elastic scattering at the analyzer crystal, which defines the energy and momentum transfer involved in

the inelastic scattering process at the sample.

IXS beamline at SPring-8

A schematic of IXS beamline (BL35XU) of SPring-8 [130] is given in Figs.3.3 (a) and (b), while Fig.3.3 (c) shows photograph of the 10m long 2θ arm of the spectrometer. The x-ray beam from the undulator source is premonochromatized with a cryogenically cooled double-crystal Si(1 1 1)

(a) Hutch Layout for BL35XU
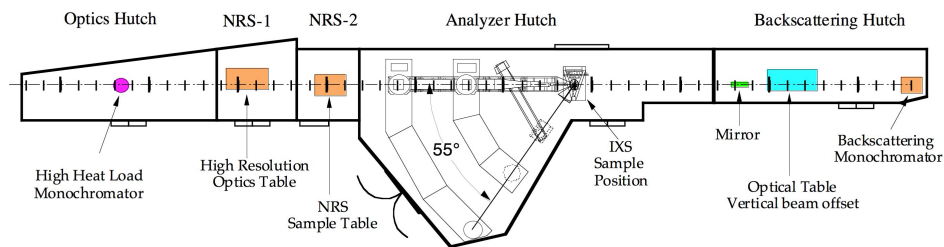
(b) Beam path for inelastic x-ray scattering
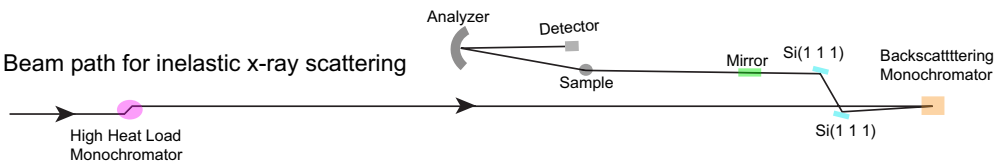
(c) 10m 2θ arm of the spectrometer
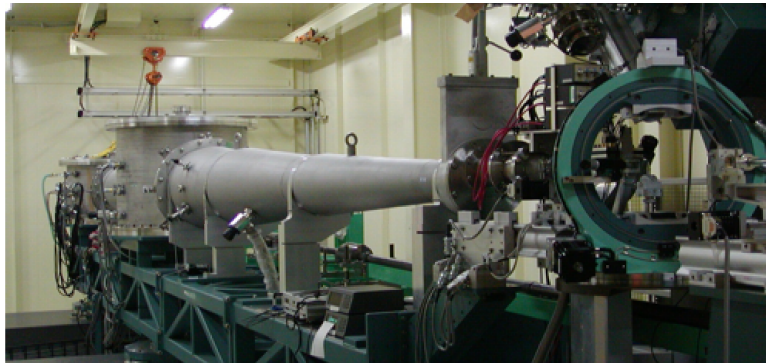
Figure 3.3: Schematic of IXS beamline (BL35XU) and photograph of the 10m 2θ arm of the spectrometer of SPring-8. (a): Hutch layout for BL35XU[130]. (b): Schematic of the beam path for IXS (vertical scattering geometry). (c): Photograph of the 10m long 2θ arm of the spectrometer of BL35XU.

Reflection	Energy (keV)	Resolution (meV)	Q_{max} (nm^{-1})	Relative flux at sample
Si(8 8 8)	15.816	6.0	74	8
Si(9 9 9)	17.794	3.0	83	2
Si(11 11 11)	21.747	1.5	101	1
Si(13 13 13)	23.725	> 0.9	111	0.2

Table 3.1: Operating parameters of BL35XU. with a 10 m long 2θ arm. Q_{max} is the maximum momentum transfers accessible with $2\theta = 55°$ [131].

monochromator to a relative bandwidth of $\Delta E/E = 1.33 \times 10^{-4}$ ($\Delta E = 3.0$ eV at 22 keV). The required high energy resolution is then obtained by main monochromator, operating at a Bragg angle θ_B of 89.98° and utilizing the Si(n n n) reflection orders. [2] This is the first axis of the triple-axis spectrometer. Due to the backscattering geometry, the reflected x-ray beam lies nearly on top of the incident beam. In order to separate them to allow enough space at the sample position, a pair of Si (1 1 1) offset crystals are used to shift the beam vertically after the backscattering monochromator.

The highly monochromatized x-ray beam ($\sim$ meV-level) is then focused onto the sample position. Samples are mounted on the goniometer, which allows for rotations about the ϕ, χ and θ axes and for translations in x, y and z directions. This is the second axis of the triple-axis spectrometer.

The scattered x-rays pass through the vacuum flight path of 10 m long 2θ arm, and are energy analyzed by spherical perfect silicon crystal analyzers at the end of the arm, operating at the same Si(n n n) reflection order as the monochromater and a Bragg angle θ_B of 89.98°. These crystal analyzers correspond to the third of the triple-axis spectrometer. The x-rays

---

[2]This backscattering configuration provides maximum angular acceptance for a given energy resolution, as can be seen by differentiating Bragg's law as, $\Delta\theta = (\Delta E/E)\tan(\theta_B)$, where E is the photon energy, θ_B is the Bragg angle for Si(n n n), and ΔE is the geometric contribution to the energy resolution due to angular divergence $\Delta\theta$.

diffracted from the analyzer crystals are recorded by corresponding independent CdZnTe detectors. Typical parameters for the instrument at BL35XU of SPring-8 are given in table 3.1. The IXS spectrometers at BL35XU and BL43LXU of SPring-8 are currently equipped with a two-dimensional (2-D) analyzer array which allows simultaneous access to a 2-D section of momentum space (see Fig.3.4). [3]

IXS scans are usually performed in a constant-$\mathbf{Q}$ mode by (1) moving the spectrometer 2θ arm so that the analyzer will intercept the scattered radiation at the momentum transfer of interest, and then (2) scanning the temperature of the monochromator while keeping the analyzers temperature fixed. This is based on the fact that a relative change of the monochromator temperature ΔT induces that of the lattice constant, $\Delta d/d = -\alpha(T)\Delta T$, which, according to Bragg's law, gives a relative change of energy $\Delta d/d = \delta E/E$, where α is the thermal coefficient of silicon. The value of α is about $2.6 \times 10^{-6} K^{-1}$ at room temperature, corresponding to, for example, ~ 18 mK/meV (56 meV/K) at 22 keV. Thus, in order to obtain the required relative energy resolution of $\Delta E/E \sim 10^{-6} - 10^{-7}$ range, it is necessary to control the temperature of both monochromator and analyzer crystals in the millikelvin regime.

3.1.5 Experimental details and data analysis procedure

Phonon measurements using IXS were performed at BL35XU[130] and BL43LXU[132] of SPring-8 in Japan. The scattered radiation was collected using a 2-D analyzer array on a 10 m horizontal 2θ arm, which allows parallelization of data collection in a 2-D section of momentum space[109]. The

---

[3]All IXS instruments presently in use employ an array of analyzer crystals, but a 2-D analyzer array exists only at BL35XU and BL43LXU of SPring-8.
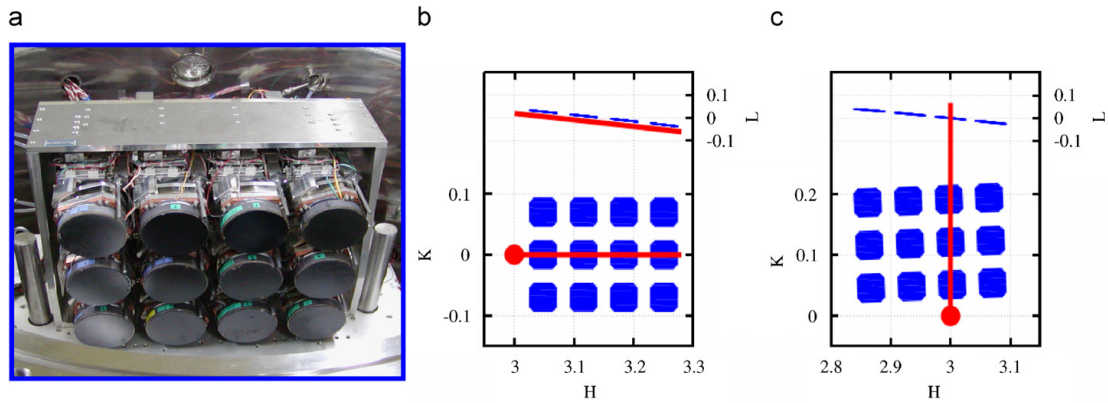
Figure 3.4: Use of the 2-D analyzer array. (Reprinted from Ref[109].) (a) shows the 4×3 array of analyzers of BL35XU at SPring-8. A 2-D analyzer array can be used to parallelize measurements of (b) longitudinal and (c) transverse phonons.

energy resolution was determined from measurements of plexiglas to be 1.5 meV - 1.8 meV at 21.747 keV (Si (11 11 11) geometry), depending on the analyzer crystals. The best fit to the experimental resolution functions was obtained by using Pseudo-Voigt profiles [Fig.3.5].

The momentum resolutions were determined by the slits in front of the crystal analyzers located 6 meters away from the sample. Setting these to 50 mm (vertical) $\times$ 50 mm (horizontal), we obtained a typical momentum resolution of 0.04 reciprocal lattice units (r.l.u.) in H and K and 0.06 r.l.u. in L. (In this thesis, $Q = (HKL)$ represents the total momentum transfers, while $q = (hkl)$ represent the reduced momentum transfer in first zone.

IXS spectra were fitted to a sum of damped harmonic oscillators (DHOs) in Eq.3.9 for several phonon modes and a resolution-limited elastic peak to account for elastic peak resulting from crystal imperfections and surface scattering. Phonon mode intensities were scaled by a detailed balance factor, and the finite resolution was accounted for by convolving in the experimentally de-

termined resolution function. The parameters (e.g., mode energies, line-width, and amplitude) were then optimized by a χ^2 fit to the data. Note that the mode energies and linewidth of the phonons reported in the thesis are deconvoluted from the experimental resolution. The χ^2-minimization and parameter error determination were performed using the Davidon-Fletcher-Powell variable metric algorithm as implemented in CERN program library, MINUIT [133]. A typical IXS spectrum is shown in Fig.3.6, where one can see elastic peak at zero energy transfer and Stokes and anti-Stokes lines of several modes due to phonon creation and annihilation. In general, low-energy phonon modes have stronger intensity than high-energy modes due to both temperature dependent thermal occupation factors and the fact that high-frequency modes
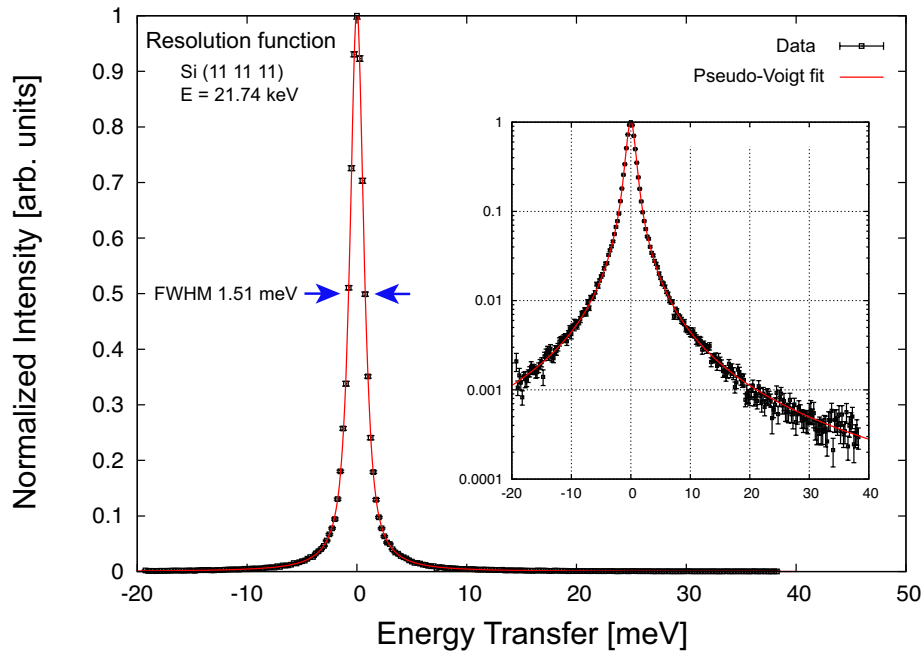
Figure 3.5: Energy scan from plexiglas sample for the determination of the energy resolution of the spectrometer at 21.747 keV (Si (11 11 11) geometry). The data are normalized to the peak intensity. The solid line is a Pseudo-Voigt fit to the data. Inset shows the resolution function on the log-scale.

have smaller displacements.

3.2   Sample preparation

3.2.1   Crystal structure and magnetic properties of $SrFe_2As_2$

Single crystals of $Sr(Fe_{1-x}Co_x)_2As_2$ with $x = 0$ and 0.08 were grown by a self flux method described in Ref. [134]. At room temperature, these compounds crystalizes in the body-centered-tetragonal $ThCr_2Si_2$-type structure with space group $I4/mmm$, as shown in Fig.3.7 (a). Throughout this thesis, we use tetragonal notation with axes along the next-nearest-neighbor iron atoms (see Fig.3.7 (b)). The tetragonal lattice parameters at room temperature are $a = b = 3.924$ Å and $c = 12.364$ Å for $x = 0$, and $a = b = 3.926$ Å
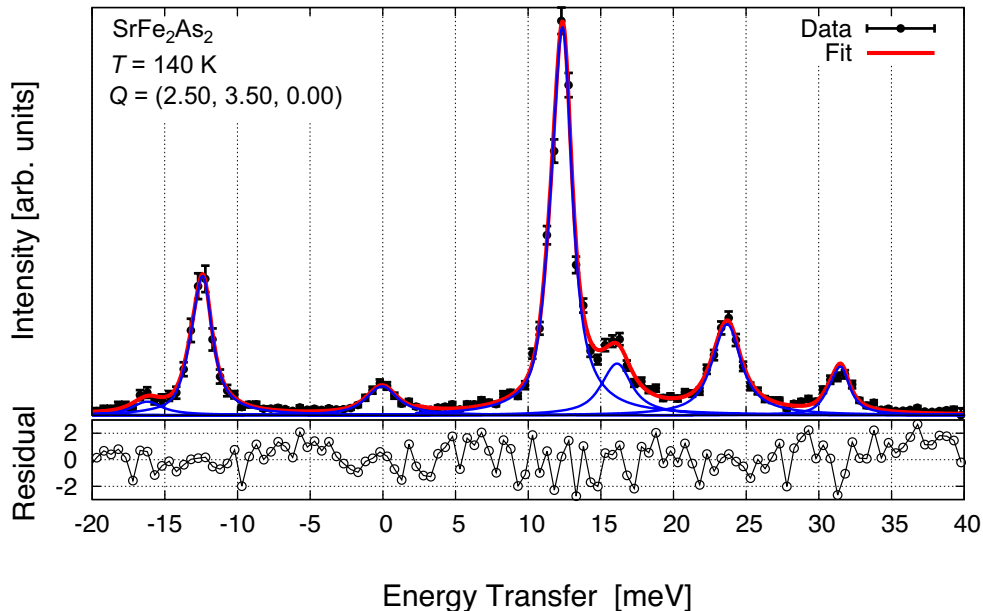
Figure 3.6: A typical IXS spectrum of $SrFe_2As_2$. (Top) IXS spectrum of $SrFe_2As_2$ at $T = 140$ K and at $\boldsymbol{Q} = (2.50, 3.50, 0.0)$. The red line is the result of the total fit, and the blue lines the individual phonons. (Bottom) Residual of the fit in standard deviation units.

and $c = 12.335$ Å for $x = 0.08$, respectively. The structural transition below $T_{s,N}$ corresponds to a tetragonal to orthorhombic transformation ($14/mmm \rightarrow Fmmm$) and the magnetic structure is collinear with the ordered moment aligned antiferromagnetically (AFM) (ferromagnetically (FM)) along the $[1\ \bar{1}\ 0]$ ($[1\ 1\ 0]$) direction corresponding to the longer a-axis (shorter b-axis) of the orthorhombic lattice (see Fig.3.7 (b). In the undoped state, $SrFe_2As_2$ exhibits simultaneous structural and magnetic phase transitions. Interestingly, Co substitution on the Fe sites splits the single transition in the undoped $SrFe_2As_2$ into two transitions. The structural (magnetic) transition temperatures, T_s
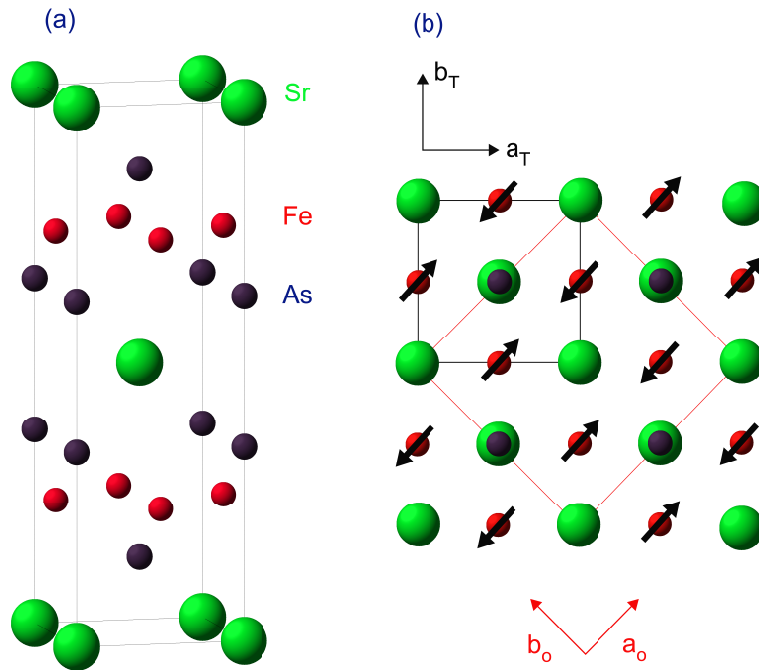
Figure 3.7: Crystallographic and magnetic structure of $SrFe_2As_2$. (a) The schematic view of the crystal structures of $SrFe_2As_2$ with the body-centered-tetragonal $ThCr_2Si_2$-type structure (space group $I4/mmm$). (b) The schematic top view of the crystal structure, and definitions of the unit cells for the high-temperature tetragonal (black line) and the low-temperature orthorhombic (red line) structures. The lattice parameters are related to each other by $a_T = b_T$, $a_o \sim b_o \sim \sqrt{2}a_T$. The directions of iron magnetic moments are indicated by arrows.

(T_N), determined from the resistivity curve of the strain-free twinned crystals are 200K (200)K and 107 ± 3 K (97) K for $x = 0$ and 0.08, respectively.

3.2.2 Methods to detwin single crystals

In the AFM phase, $SrFe_2As_2$ naturally forms small twin domains, corresponding to alternation of the orthorhombic a- and b- axes[135] (see Fig.3.8 (a)). For any experiments probing on length scales greater than the typical domain size ($\sim 10 - 50\mu$m)[135], this effect obscures intrinsic anisotropic properties below $T_{s,N}$, and it is therefore necessary to detwin single crystals to make an in-plane anisotropy measurements. Two different methods have been employed so far to detwin single crystals *in situ*, including (1): application of uniaxial stress (either compressive [16, 81, 82, 83] or tensile[136]), (2): application of in-plane magnetic field[137]).

For the present study, we have designed a mechanical detwinning device to allow IXS measurements under compressive uniaxial pressure. Since the orthorhombic a and b axes are oriented at 45° to the tetragonal $a(b)$-axis (Fig.3.7 (b)), crystal was cut into a square shape, with the tetragonal $a(b)$-axis oriented at 45° to the edges of the crystal in order to apply uniaxial stress along the orthorhombic $a(b)$ directions. The crystal was glued between two copper prongs (similar to a tuning fork) with a screw used to carefully adjust the pressure parallel to one [1 1 0] direction (see Fig.3.8 (c)). Application of the uniaxial pressure makes it favorable to align domains with their shorter b_o-axis along the pressure, giving rise to an increased volume fraction of one domain orientation over the other (Fig. 3.8 (b)) [4].

---

[4]Note that the longer a_o-axis is favored in the case of tensile stress[136].
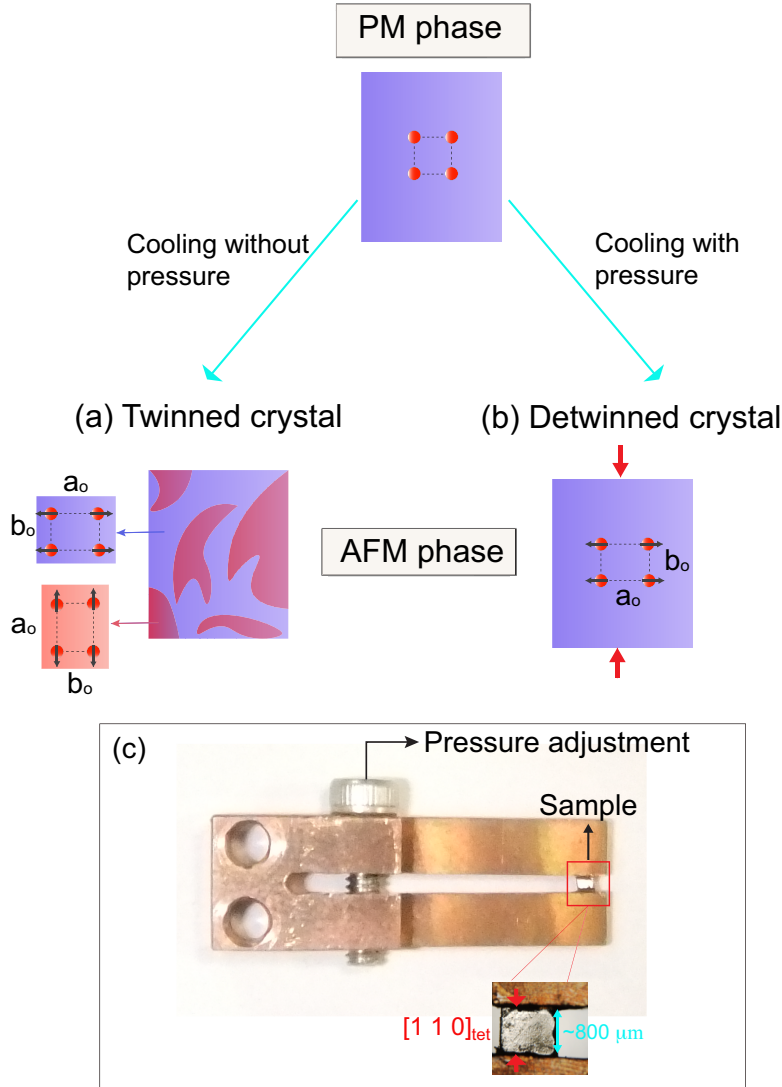
Figure 3.8: The experimental methods to mechanically detwin single crystals *in situ*. (a) In the AFM phase, iron-pnictides materials generally form small twin domains. The arrows mark the moment directions of iron . (b) Application of the uniaxial pressure favors one twin orientation (blue) over the other (red), with the shorter orthorhombic b axis along the applied pressure. (c) The mechanical device used to detwin single crystals *in situ*. At an incident x-ray energy of 21.474 keV, the penetration depths for $SrFe_2As_2$ is about 100μm, which, for our thin samples, allows IXS measurements with transmission (Laue) geometry for many $\mathbf{Q}$ points.

Chapter 4

Experimental Results

4.1 Phonon anisotropy observed for detwinned $\mathbf{Sr(Fe_{1-x}Co_x)_2As_2}$

In this chapter we present the results of meV-resolved IXS measurements on $Sr(Fe_{1-x}Co_x)_2As_2$ with $x = 0$ and $x = 0.08$. The IXS data were collected in transverse geometries along two tetragonally-equivalent lines corresponding to the two $\Gamma - M$ directions: (1) $\boldsymbol{Q} = (3 - q, 3 + q, 0)$ with $\boldsymbol{q} = (-q, q, 0)$ parallel to the AFM ordered direction (Fig. 4.1 (a)); (2) $\boldsymbol{Q} = (3 - q, -3 - q, 0)$ with $\boldsymbol{q} = (-q, -q, 0)$ parallel to the FM ordered direction (Fig. 4.1 (b)). One should note that these two $\Gamma - M$ directions become inequivalent in the AFM phase.

4.1.1 IXS measurements on $SrFe_2As_2$

In the AFM phase, $SrFe_2As_2$ generally forms small twin domains, which obscure its intrinsic anisotropic properties. To avoid twinning, we applied
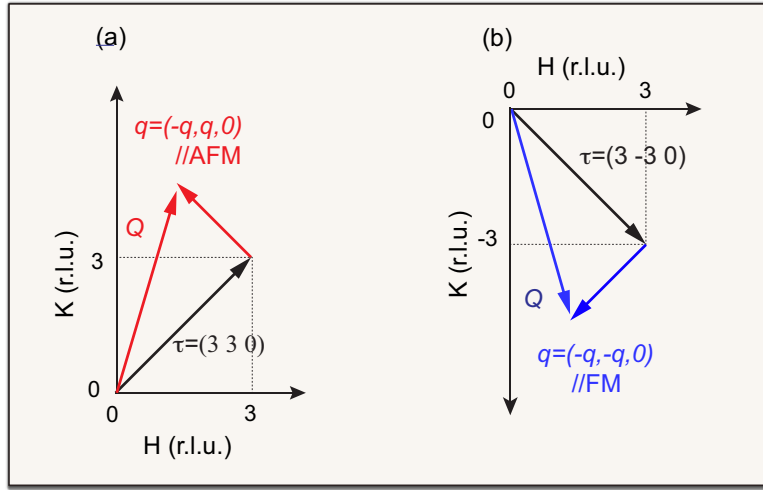
Figure 4.1: Schematic diagrams illustrating scattering geometry in reciprocal space. (a) and (b) indicate the positions in reciprocal space where IXS scans were measured. In the AFM state, these two scans correspond to inequivalent $\Gamma - M$ directions, pointing along the antiferromagnetic and ferromagnetic directions of the Fe-Fe bonds, respectively

uniaxial compressive pressure to a crystal before cooling below $T_{s,N}$, as described in Sec 3.2.2. For a twinned crystal, Bragg reflections of the tetragonal $(h, h, 0)$ type exhibit splitting in 2θ corresponding to two distinct d-spacings (see Fig.4.2 (a)). Application of uniaxial pressure along [1 1 0] direction favors one twin over the other as can be seen in Fig. 4.2 (b).

In Figs. 4.2 (c) and (d), we compare IXS spectra at $\boldsymbol{q} = (0.5, \pm 0.5, 0)$ for twinned and detwinned $SrFe_2As_2$ crystals in the AFM ordered state. For the twinned crystal in Fig. 4.2 (c), there is no clear evidence for any change between two tetragonally-equivalent momentum positions due to the twinning, except for a tiny (~ 0.1 meV) energy shift of some of the modes. However, once detwinned, clear phonon anisotropy can be observed as easily seen in Fig.4.2 (d), where both the frequencies and intensities of the modes change. This is in sharp contrast with the data from twinned crystals, including previous related works on $BaFe_2As_2$[97] and $PrFeAsO_{1-x}$[95], which shows isotropic
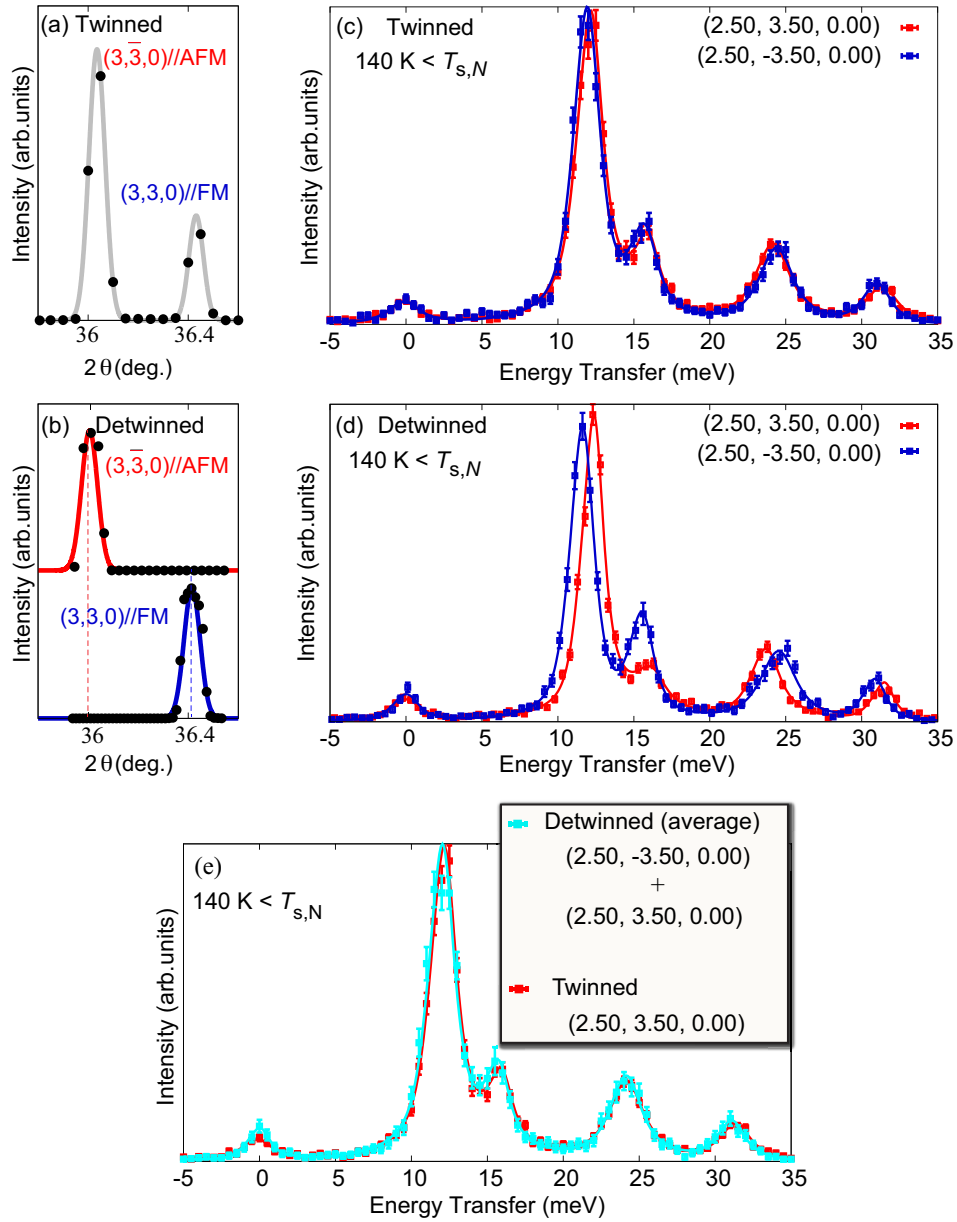
Figure 4.2: Anisotropy of phonon structure of detwinned SrFe$_2$As$_2$. (a) and (b), Typical 2θ scan of the tetragonal $(3\,3\,0)$ and $(3\,\bar{3}\,0)$ reflections for twinned and detwinned crystals below $T_{s,N}$. (c) and (d), IXS spectra for twinned and detwinned crystals at $\boldsymbol{Q} = (2.5, \pm 3.5, 0)$ measured below $T_{s,N}$. Solid lines are fits to the data. (e) Comparison of IXS spectra measured on the twinned crystal and a superposition of two IXS spectra measured on the detwinned crystal.

phonon structure in the AFM phase.

Given that our IXS measurements are performed under uniaxial pressure, it is important to examine whether our detwinning method affects the intrinsic phonon structure of the crystal. Figure 4.2 (e) compares IXS spectrum at $q = (0.5, 0.5, 0)$ in zero pressure (red) and average of the two IXS spectra at $q = (0.5, \pm0.5, 0)$ under uniaxial pressure (cyan). One can see that IXS spectra measured on twinned crystal can be reproduced by averaging those measured on detwinned crystal, as expected from domain mixing. This confirms the intrinsic anisotropy of phonon structure in the AFM phase. Furthermore, in one case, we were able to observe the phonon anisotropy even without the application of external pressure (see Fig.4.3 (c)) when we were fortunate enough to isolate a relatively twin-free section of a crystal as can be seen in Figs.4.3 (a) and (b), where comparison of the integrated intensity between $(3, 3, 0)$ and $(3, \bar{3}, 0)$ Bragg reflections shows that relative volume fraction of the larger domain is approximately 70% of the sample volume illuminated by the x-ray beam. The resulting relatively twin-free structure was not stable when the temperature was cycled, so most experiments were carried out under pressure. However, the fact that the same phonon anisotropy was observed without pressure suggests that the pressure does not significantly affect the response of these samples.

The momentum dependence of the changes observed across $T_{s,N}$ are shown in Fig.4.4. Above $T_{s,N}$, IXS spectra are essentially identical in the two Γ-M directions [see Fig. 4.4 (a)], as the crystal has C_4 rotational symmetry in tetragonal paramagnetic (PM) phase. In contrast, on lowering temperature below $T_{s,N}$, which breaks the C_4 rotational symmetry, anisotropic phonon shifts develop between two Γ-M directions (see Fig.4.4 (b)). No signif-
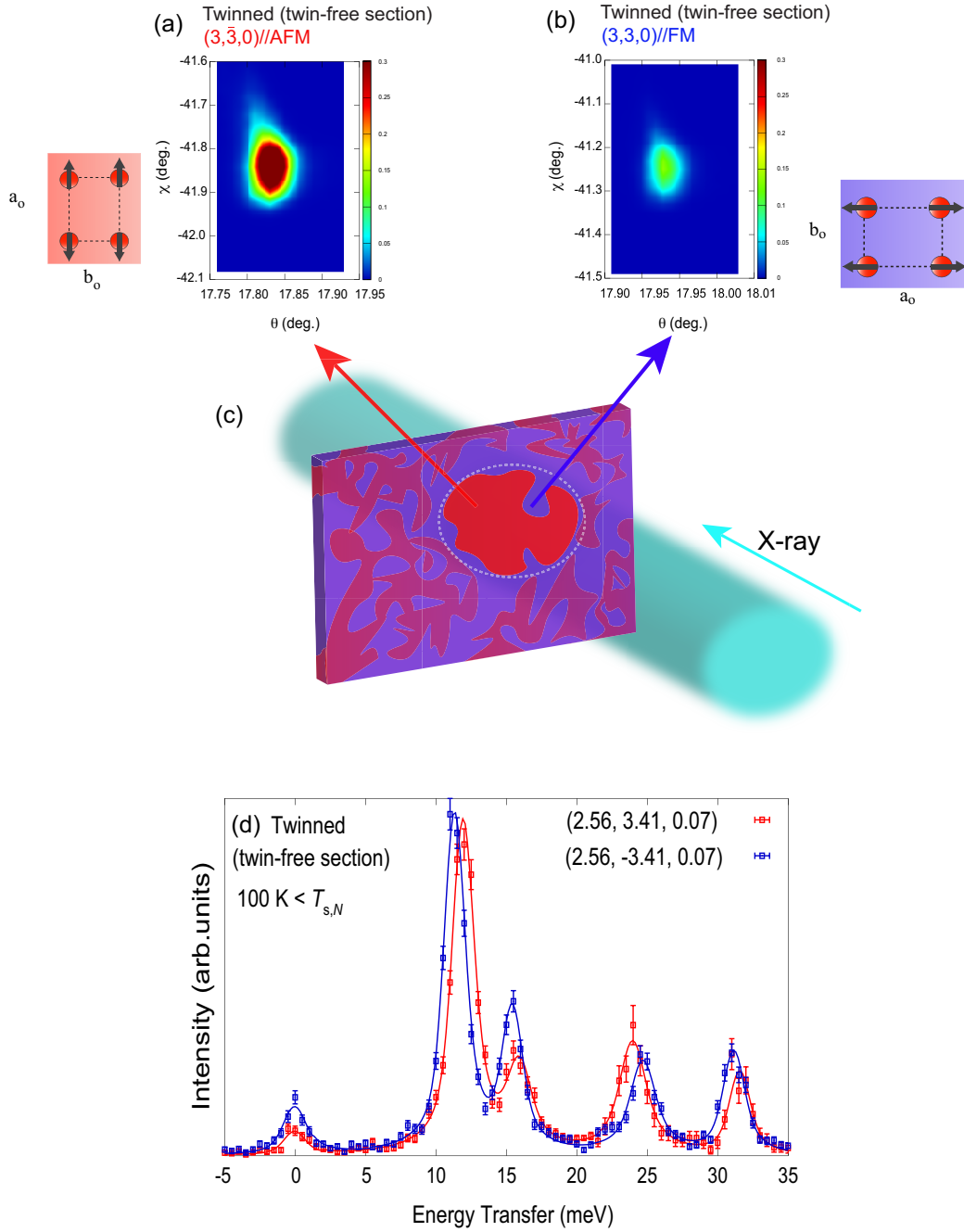
Figure 4.3: Anisotropy of phonon structure of strain-free twinned crystal. (a),(b) Two-dimensional profiles of the $(3,3,0)$ and $(3,\bar{3},0)$ reflections for strain-free twinned crystal. θ-χ scans were performed on the same sample position, with 2θ values corresponding to $(3,\bar{3},0)$ and $(3,3,0)$, respectively. Comparison of the integrated intensity between these two Bragg reflections shows that the relative volume fraction of the larger domain is approximately 70 % of the sample volume illuminated by the x-ray beam. (c) Schematic illustration of the measurement on a crystal with relatively twin-free section. (c) IXS scans at this position shows clear phonon anisotropy without the application of external pressure.

icant change in line-width was observed across $T_{s,N}$ (*e.g.*, full-width at half-maximum (FWHM) of the 24 meV mode at $q = 0.50$ is 0.70 ± 0.10 meV for 140 K and 0.74 ± 0.09 meV for 210 K). Note that the small orthorhombic structural distortion $((a - b)/(a + b) \sim 0.5$ %$)$ is expected to have only a
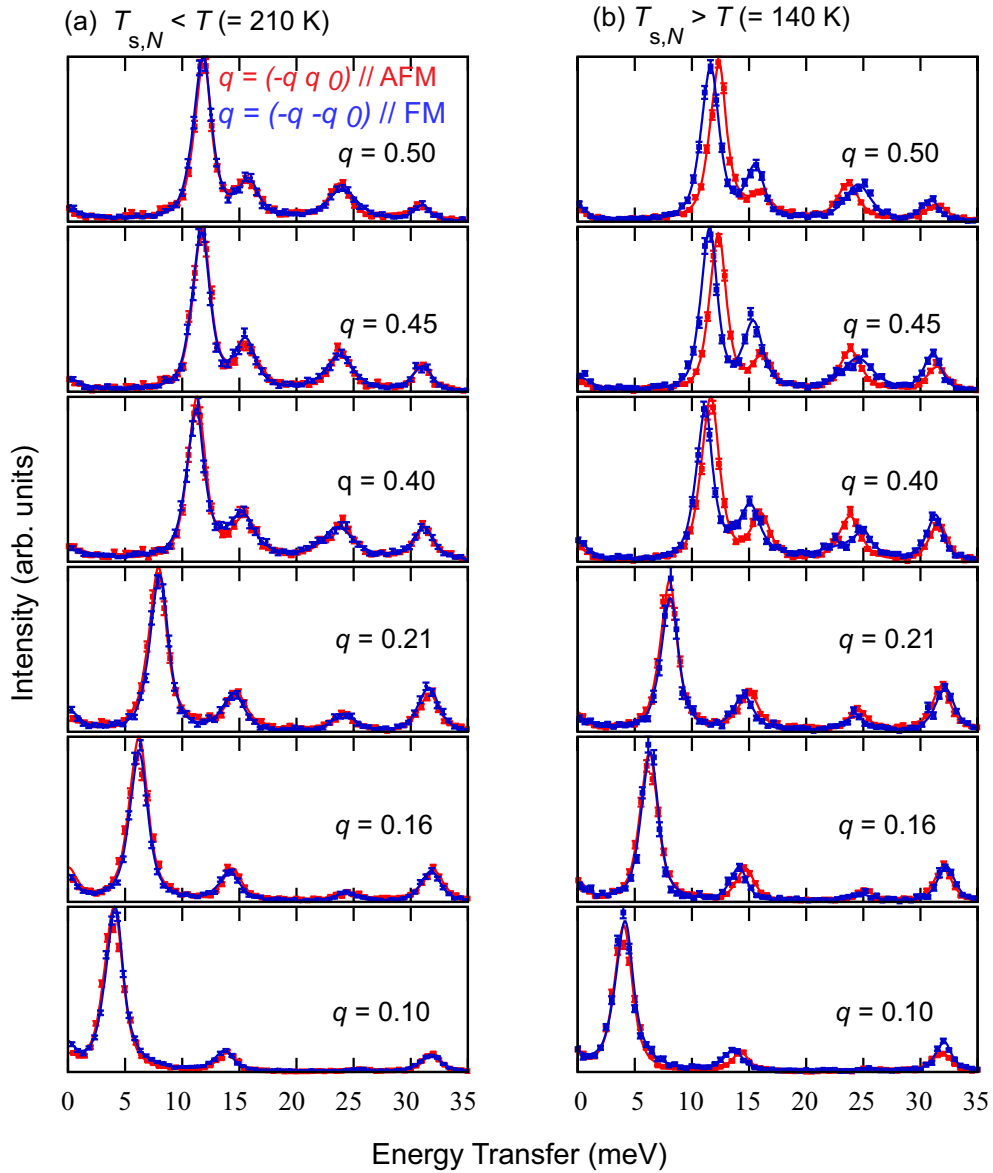
Figure 4.4: (a),(b) Temperature dependence of IXS spectra of detwinned $SrFe_2As_2$ at $\boldsymbol{Q} = (3 - q, 3 + q, 0)$ (red) and $\boldsymbol{Q} = (3 - q, -3 - q, 0)$ (blue) corresponding to the two Γ-M directions.

very small direct effect on the phonons between the two Γ-M directions[97]. We therefore expect that the changes in the phonon energies are predominantly the result of the onset of the magnetic order, as opposed to the small orthorhombic structural distortion[1].

4.1.2 IXS measurements on Sr(Fe$_{0.92}$Co$_{0.08}$)$_2$As$_2$

We also performed IXS measurements on underdoped Sr(Fe$_{0.98}$Co$_{0.08}$)$_2$As$_2$ with $T_s = 107 \pm 3$ K and $T_N = 97$ K determined by zero-pressure transport measurement. A remarkable property of this compound is the separation between T_s and T_N, which is not present in the parent phase of 122 family of iron-pnictides where the two transitions occur simultaneously. The extended temperature window above T_N allows, in principle, one to distinguish the effects of the two phase transitions on phonon response. However, the mechanical pressure necessary to detwin the crystals induces a significant increase in T_s and T_N[138]. This makes it difficult to access the narrow temperature range $T_s > T > T_N$, as the AFM phase transition cannot be determined by x-ray diffraction. Recently, it has been shown that similar uniaxial pressure used to detwin the crystals has a very small effect on T_s and T_N for the annealed crystals. [139]. In the current study, we therefore used annealed single crystal of Sr(Fe$_{0.92}$Co$_{0.08}$)$_2$As$_2$ in order to avoid the effect of uniaxial pressure on the structural and magnetic phase transitions. In fact, the (3,3,0) Bragg reflection as a function of temperature shows $T_s \sim 110$ K (see Fig.4.5), in agreement with the value found in zero-pressure transport measurement. We thus do not observe any significant modification of T_s within the experimental accuracy, consistent with Ref[139].

---

[1]This will be confirmed in Sec.4.1.2.

IXS measurements were performed at three temperature regimes as indicated by arrows in Fig.4.5: (1) $T = 125K > T_s$, (2) $T_s > T = 103K > T_N$ and (3) $T_N > T = 83K$. Representative IXS scans for $Sr(Fe_{0.92}Co_{0.08})_2As_2$ at $\boldsymbol{q} = (0.5, \pm0.5, 0)$ are shown in Fig.4.6. In a tetragonal PM phase at $T > T_s$, IXS spectra are essentially identical in the two $\Gamma - M$ directions, respecting C_4 symmetry (see Fig.4.6 (a)). In the orthorhombic PM state at $T_s > T > T_N$, the orthorhombic structural distortion lifts the degeneracy between these two directions. However, as shown in Fig.4.6(b), for the phonon spectra, there is essentially no anisotropy between them within the experimental accuracy. As mentioned earlier, we expect that the orthorhombic distor-
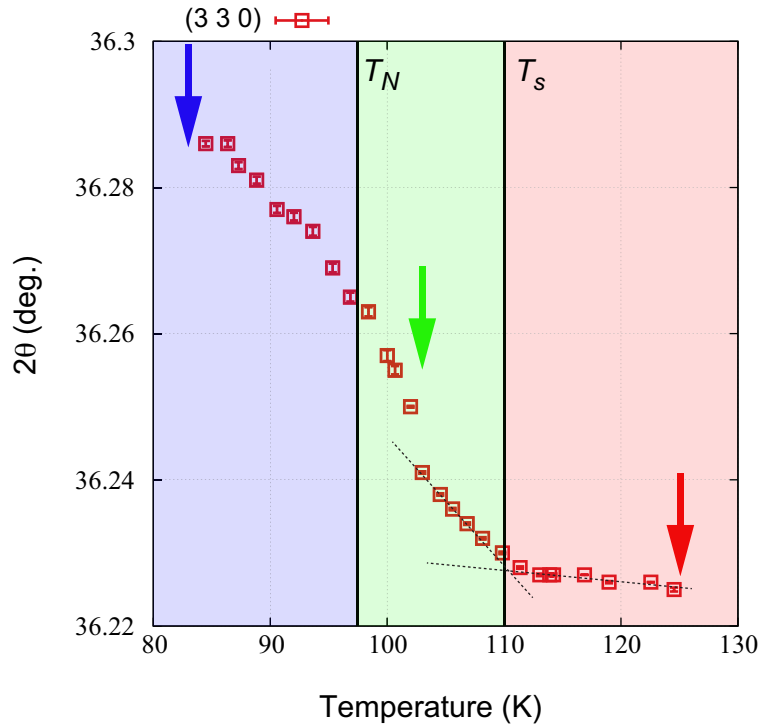
Figure 4.5: 2θ angle of (3,3,0) Bragg reflection as a function of temperature in detwinned $Sr(Fe_{0.92}Co_{0.08})_2As_2$. The dotted line is a guide to the eye. Note that T_N was determined from transport measurement. Arrows indicate the temperatures where IXS scans were performed.
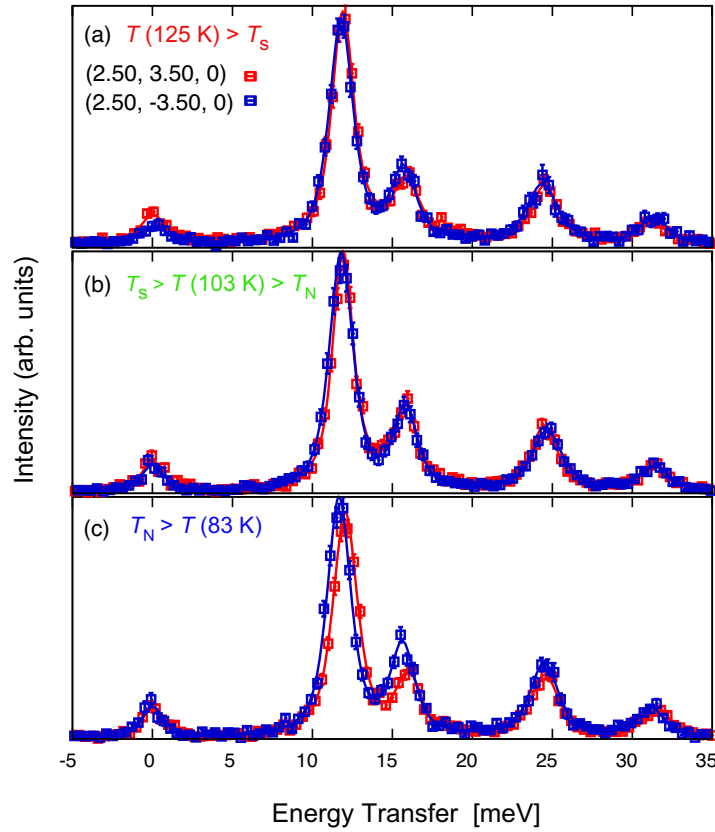
Figure 4.6: Anisotropy of phonon structure of detwinned $Sr(Fe_{0.96}Co_{0.08})_2As_2$ at $\boldsymbol{q} = (0.5, \pm0.5, 0)$. IXS scans were performed at temperatures indicated in Fig.4.5 by arrows. (a) $T = 125K > T_s$, (b) $T_s > T = 103K > T_N$ and (c) $T_N > T = 83K$.

tion in iron-pnictides is too weak to be directly resolved as the splitting of phonon modes at tetragonally-equivalent momentum positions. One can see clear anisotropy only below T_N, where the long-range AFM order sets in (see Fig.4.6 (c)). This result supports our interpretation that C_4 to C_2 symmetry change in phonon dispersion is predominantly the result of the AFM order that breaks the C_4 rotational symmetry of the underlying crystalline lattice. [2]

---

[2]We note that, in contrast to incipient nematicity above T_s, as has been demonstrated by several recent experiments[16, 140], the anisotropy in phonon structure appears only when C_4 symmetry is broken by the static AFM order. In this respect, our results suggest that nematic fluctuations in the tetragonal phase are, indeed, too weakly coupled to phonons to be detected.
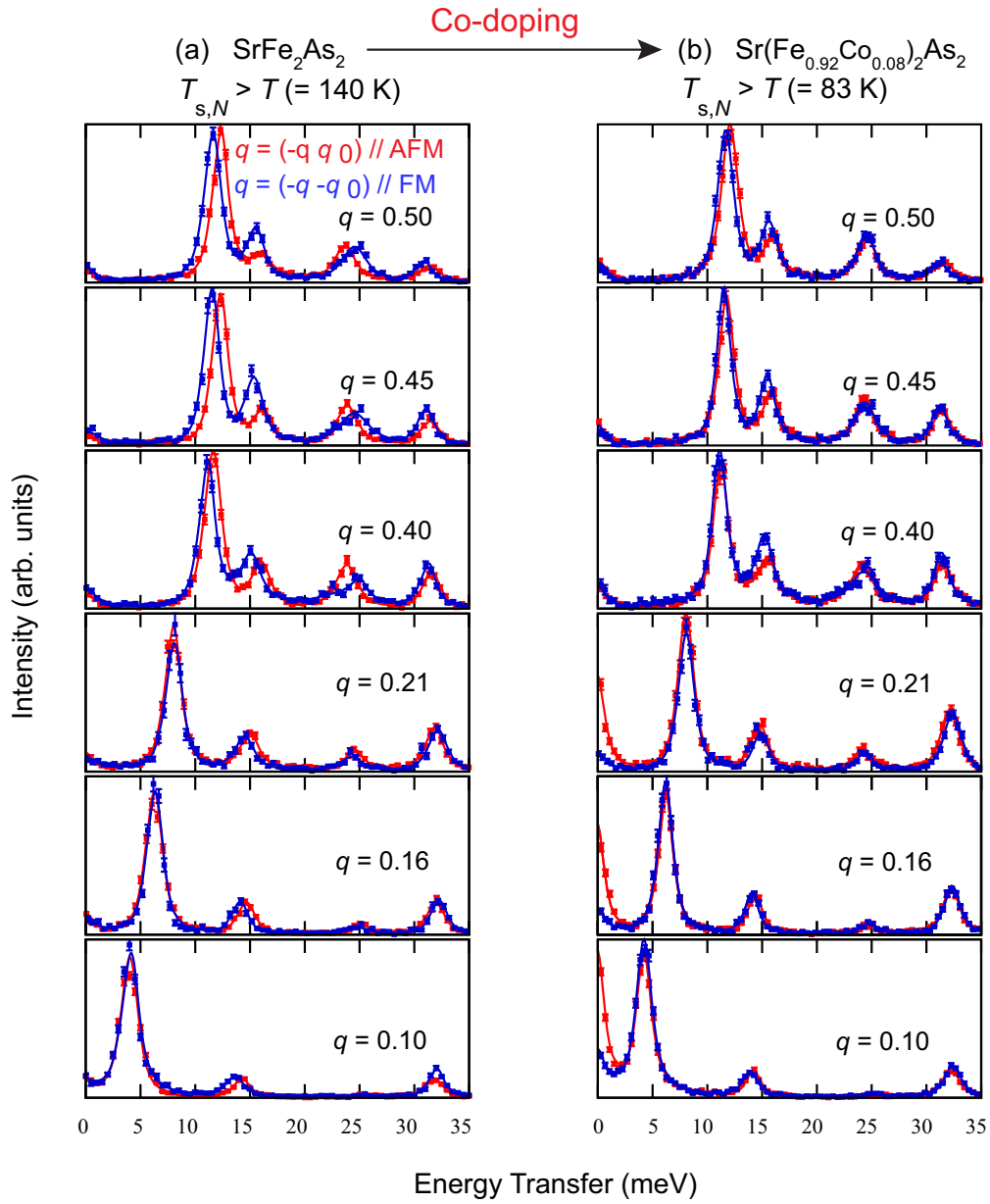
Figure 4.7: Comparison of IXS scans for parent $SrFe_2As_2$ and underdoped $Sr(Fe_{0.98}Co_{0.08})_2As_2$ in the AFM phase along the two $\Gamma - M$ high-symmetry lines $\boldsymbol{Q} = (3 - q, 3 + q, 0)$ (red) and $\boldsymbol{Q} = (3 - q, -3 - q, 0)$ (blue)

Another important observation is that anisotropy in phonon structure is significantly reduced upon Co-doping. This is evident in Fig.4.7, where IXS scans for both parent and doped materials show a similar anisotropy char-

acterized by mode splitting and intensity changes of some modes, but the magnitude of mode splitting for doped material is significantly reduced over the entire Brillouin zone. Since this observation follows the same trend as the AFM order that is suppressed upon doping, it is reasonable to associate the changes observed for doped material to the reduction of the ordered Fe moment. Similar doping-induced suppression of mode splitting was also found in Raman active ($q = 0$) optical mode[106], consistent with the present work.

4.2 Comparison with DFT calculations

We now compare the phonon dispersion against DFT calculations. DFT calculations for $SrFe_2As_2$ were performed using the relaxed tetragonal structure ($I4/mmm$) with generalized gradient approximation (GGA) using projector-augmented wave (PAW) pseudopotentials, as implemented in the Vienna *ab-initio* Simulation Package (VASP)[141, 142, 143]. Phonons were calculated using a direct method [144] for both nonmagnetic and magnetic ground states. The resulting mode energies and polarization vectors were used to compute the dynamical structure factor within the limit of single-phonon scattering based on Eq. 3.8. As discussed in Sec.3.1.3, the phonon intensity depends on the total momentum transfer Q, rather than the reduced momentum transfer $q = Q - \tau$, where τ is the nearest Bragg vector to Q. This means that phonon modes at a specific reduced wave vector q have different intensities in different Brillouin zones, but they have the same energies and linewidths. It is therefore worthwhile to perform lattice dynamics calculations prior to the experiments in order to find where it is easiest to separate the mode of interest from other modes.
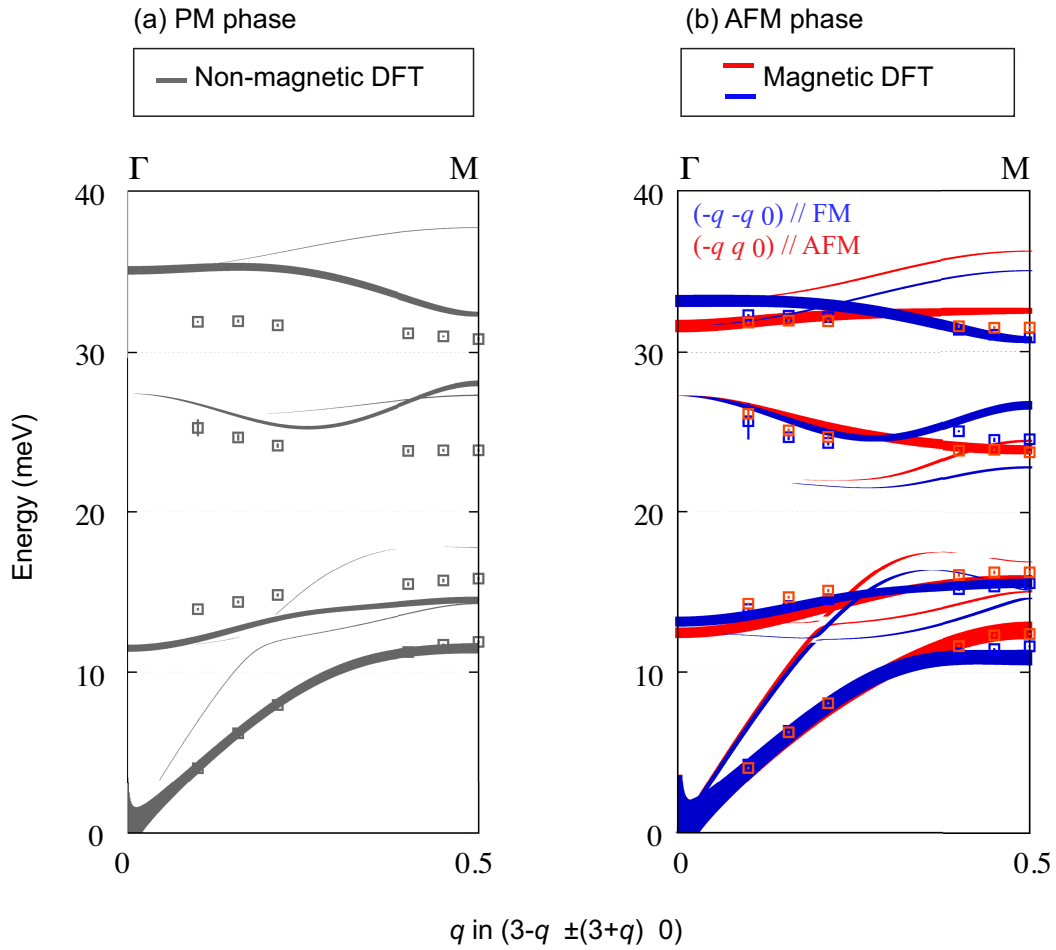
Figure 4.8: Comparison of the measured dispersion for detwinned $SrFe_2As_2$ and DFT calculations for (a) non-magnetic and (b) magnetic ground states along two $\Gamma - M$ lines, $\boldsymbol{Q} = (3 - q, \pm(3 + q), 0)$. In the AFM state, these two $\Gamma - M$ directions become inequivalent, pointing along the AFM (red) and FM(blue) directions of the Fe-Fe bonds, respectively. Lines represent calculated phonon dispersions weighted by the dynamical structure factor, whereas the data points represent experimental phonon energies.

Fig. 4.8 shows the results of calculations and the data from the detwinned crystal of $SrFe_2As_2$ along two $\Gamma - M$ lines $\boldsymbol{Q} = (3 - q, \pm(3 + q), 0)$. Lines represent calculated phonon dispersions weighted by the dynamical structure factor, while the data points represent experimental phonon energies. The non-magnetic DFT calculation (grey curve in Fig.4.8 (a)) shows poor agreement
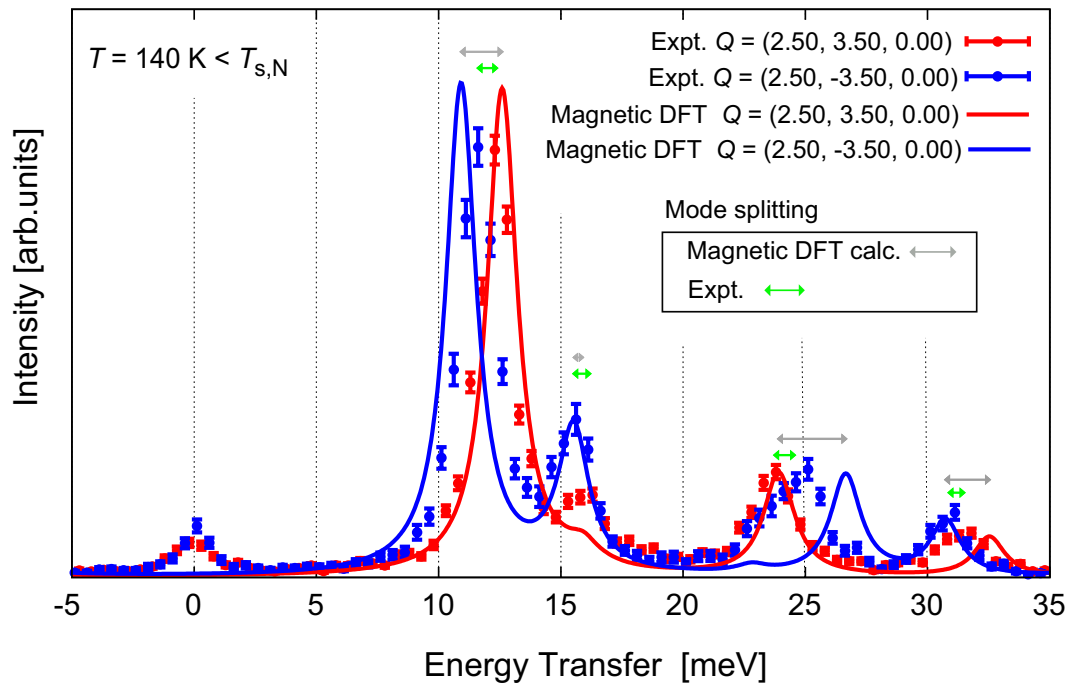
Figure 4.9: Comparison of the experimental and calculated IXS spectra for SrFe$_2$As$_2$. The solid lines are results of magnetic DFT calculation, convoluted with the instrumental resolution. The double-sided arrows represent the magnitude of mode splitting obtained from the experiment (green) and DFT calculation (grey).

with the experimental data, especially for the branch dispersing from ~ 35 meV at Γ point. The calculated energy of this branch is significantly higher than observed. The calculations can be brought into better agreement with the data if magnetism is included in the calculations (see the red and blue curves in Fig.4.8 (b)), as suggested by the earlier works [94, 95, 97, 104]. In general, magnetism has the biggest effect on some high energy branches, with lower energy branches relatively unaffected. Note that the change in relative intensity for the modes at ~ 15 meV in the AFM phase is also reproduced by magnetic DFT calculations as shown in Fig.4.9. However, the magnetic

calculations predict splitting of modes that is much larger than we observe. This is evident in Figs. 4.8 (b) and 4.9, where the magnetic calculations give mode splitting of several meV near zone boundary, while our data shows splitting of ~ 1 meV at most[3].

---

[3]The magnetic DFT calculations for the relaxed orthorhombic structire sliightly improve the overall agreement with the data, but is clearly inadequate[95].

Chapter 5

Discussion

5.1 Comparison with modified models

5.1.1 Modification to force constant matrices

To gain insight into our results, we consider a phenomenological modification to the real space force-constant (FC) matrices. We decompose the magnetic FC matrices into parts obeying C_4 (tetragonal) and C_2 (magnetic) rotational symmetry as $\phi_{ld\alpha,l'd'\beta} = \phi^{C_4}_{ld\alpha,l'd'\beta} + \phi^{C_2}_{ld\alpha,l'd'\beta}$ where α and β are the cartesian directions, and d and d' specify a pair of atoms in unit cell l and l', respectively. The symmetry-recovered C_4 matrices $\phi^{C_4}_{ld\alpha,l'd'\beta}$ are obtained by averaging tetragonally-equivelent matrices in the magnetic DFT. A similar symmetrization procedure has also been used to compute the FC matrices of iron in the high-temperature PM phase[145]. We then reconstruct the effective FC matrices $\phi^{\text{eff}}_{ld\alpha,l'd'\beta}$ by scaling C_2 term $\phi^{C_2}_{ld\alpha,l'd'\beta}$ linearly in λ,

$$\phi^{\text{eff}}_{ld\alpha,l'd'\beta} = \phi^{C_4}_{ld\alpha,l'd'\beta} + \lambda\phi^{C_2}_{ld\alpha,l'd'\beta} \tag{5.1}$$
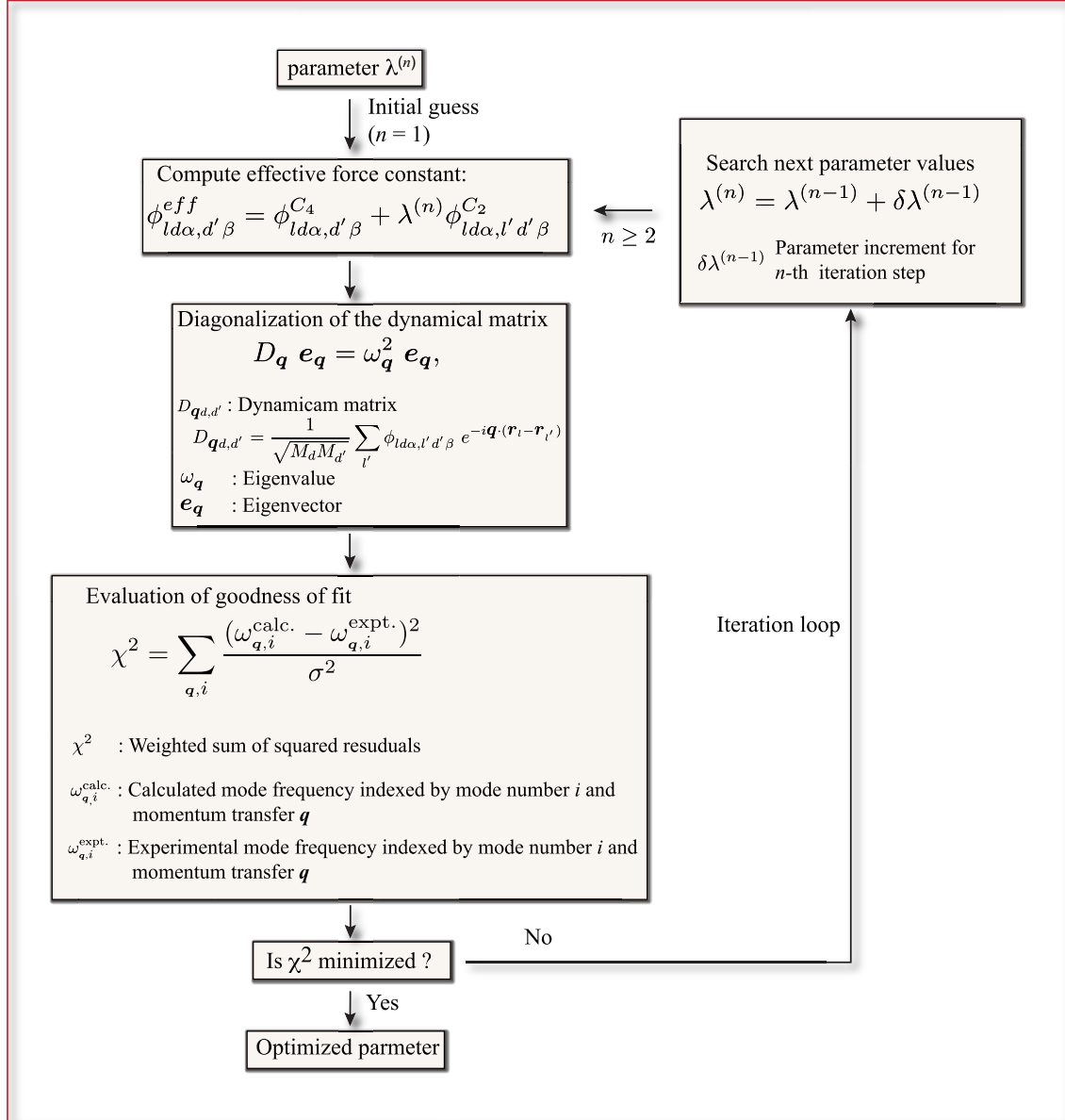
Figure 5.1: Flow chart showing the procedures used for the parameter optimization of the model in Eq.5.1. The χ^2-minimization were performed by CERN program library, MINUIT[133]. The standard formalism for lattice dynamics is summarized in Appendix A.

where λ is a scaling factor that accounts for renormalization of the FC anisotropy. The optimal value of λ in the AFM phase is determined to be 0.35 ± 0.05 by numerical optimization of the magnitude of mode splitting ΔE to match the measured values at each momentum transfer. (For details of the parameter optimization procedure, see flow chart in Fig.5.1.) We also considered a model where $\phi^{C_2}_{ld\alpha,l'd'\beta}$ exponentially decays with length between a pair of atoms, but the best fit was obtained with the uniform linear scaling in Eq. 5.1. This, as well as the fact that we observe similar mode splitting at both high and low q regions, indicates that there is not any characteristic length scale to the renormalization of FC anisotropy.

The resulting rescaled magnetic DFT calculation with $\lambda = 0.35$ (see Fig.5.2 (b)) shows better overall agreement with the data for parent $SrFe_2As_2$ than the original DFT calculations (see Fig.5.2 (a)) [1]. This can also be seen in Figs.5.2 (c) - (f), where the momentum dependence of the calculated mode splitting is shown in comparison with the experimental data. With a linear rescaling of FC anisotropy using Eq.5.1, the calculated mode splitting can be reduced to the level of the experimental data, except for mode 2 at ~ 14 meV (see Fig.5.2 (d)).

We also applied the same fitting procedure to the results obtained from Co-doped $Sr(Fe_{0.92}Co_{0.08})_2As_2$, where we observe the reduced anisotropy in phonon structure. Numerical optimization yields a scaling factor λ of 0.097 for this doped material. The results of fits to the experimental data are shown in Fig.5.3, where one can see that the calculation can be brought into much closer agreement by rescaling the FC anisotropy. Thus, the model in Eq.5.1 is in reasonable agreement with the experimental data for both parent and

---

[1]$\lambda = 1$ in Fig5.2 (b) corresponds to the FC matrices obtained from the original magnetic DFT calculation
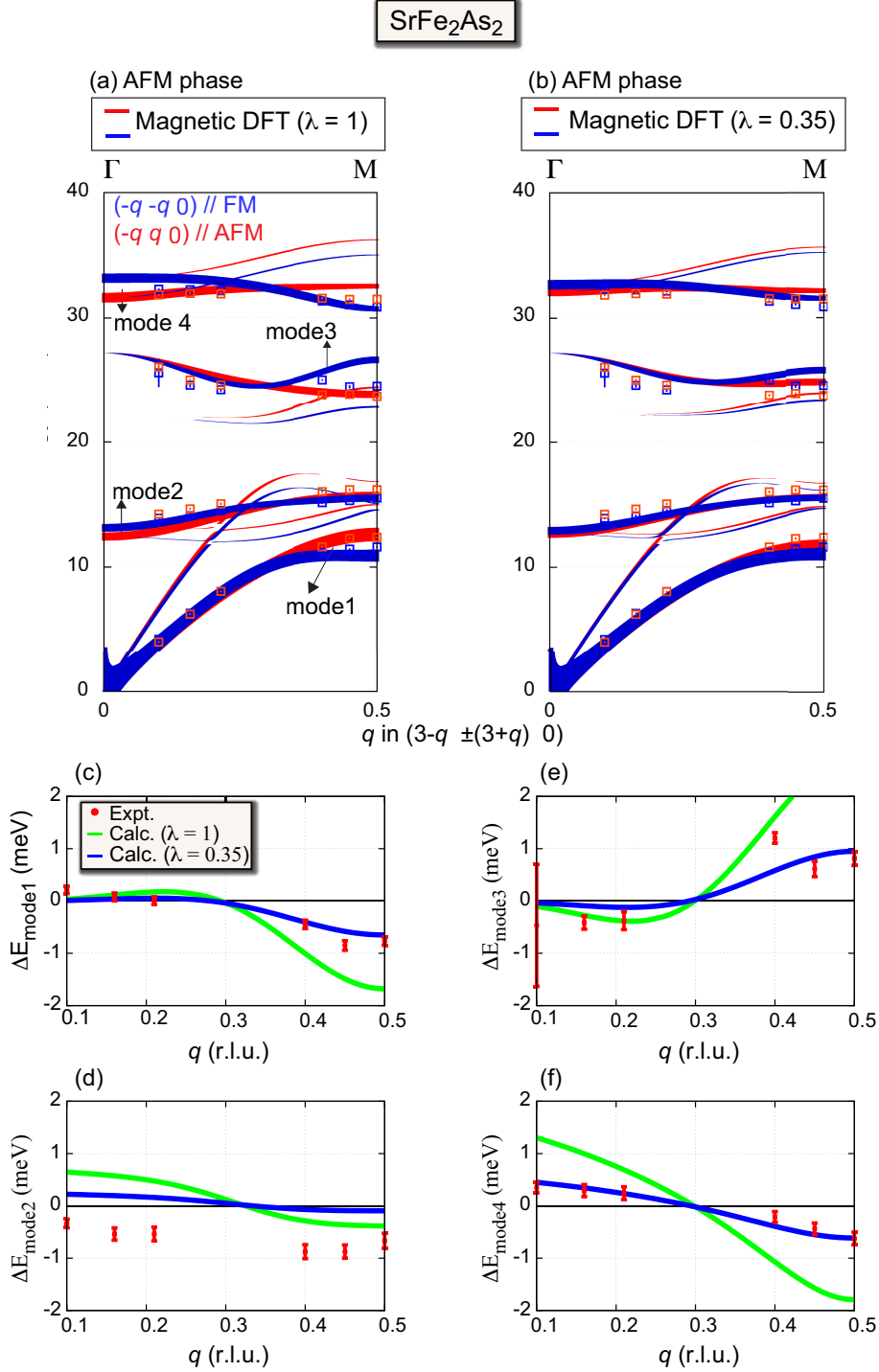
Figure 5.2: Comparison of the measured dispersion for detwinned $SrFe_2As_2$ and modified DFT calculations at $\boldsymbol{Q} = (3-q, \pm(3+q), 0)$: (a) original magnetic DFT calculation, (b) rescaled magnetic DFT calculation. (d)-(g) Comparison of the measured mode splitting for detwinned $SrFe_2As_2$ and DFT calculations at $\boldsymbol{Q} = (3-q, \pm(3+q), 0)$. Mode1 is the TA mode, modes 2, 3, and 4 have, respectively, E_u, B_{1g}, and E_u symmetry at Γ in the tetragonal structure ($I4/mmm$).
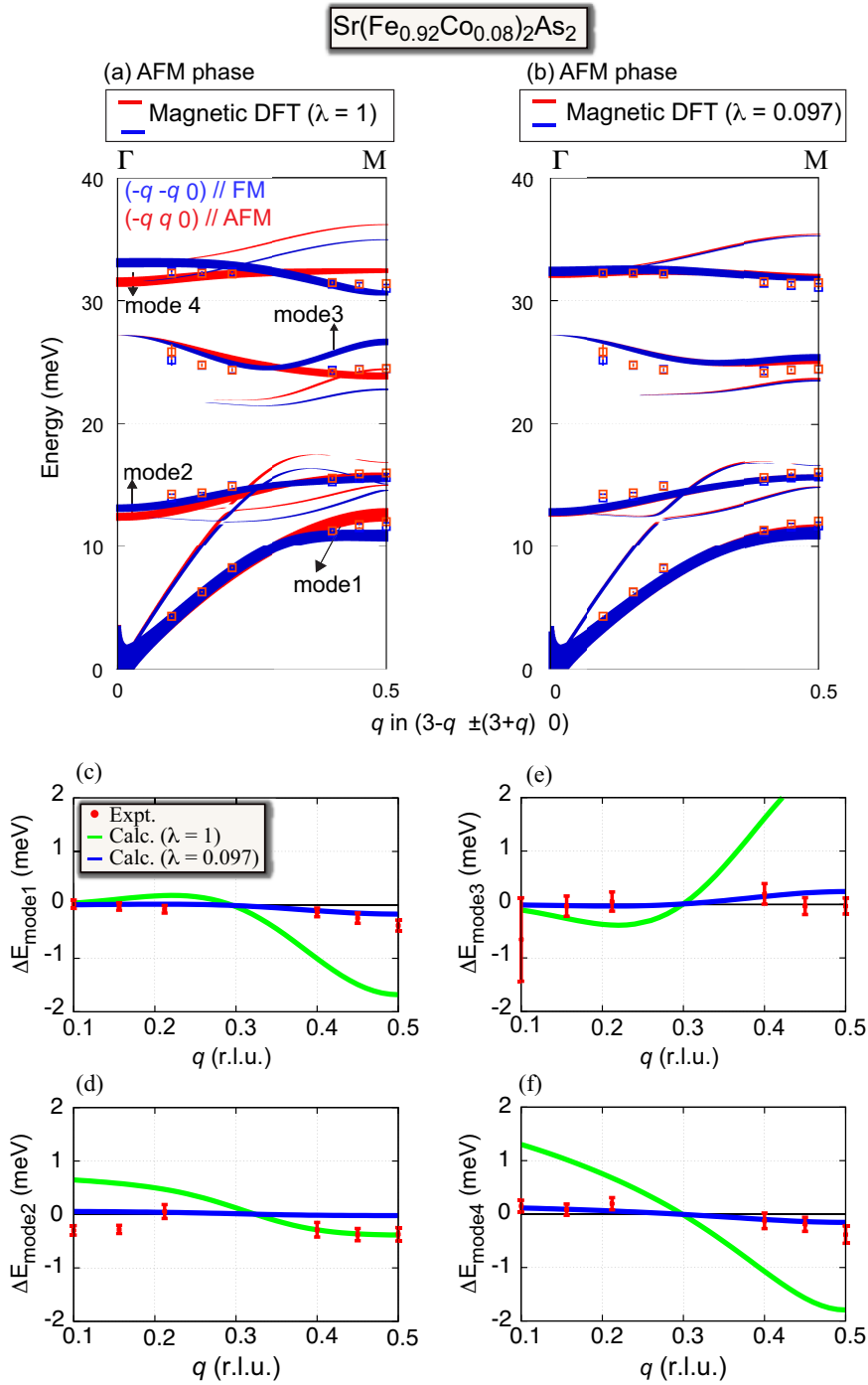
Figure 5.3: Comparison of the measured dispersion for detwinned $Sr(Fe_{0.92}Co_{0.08})_2As_2$ and modified DFT calculations at $\boldsymbol{Q} = (3-q, \pm(3+q), 0)$: (a) original magnetic DFT calculation, (b) rescaled magnetic DFT calculation. (d)-(g) Comparison of the measured mode splitting for detwinned $Sr(Fe_{0.92}Co_{0.08})_2As_2$ and DFT calculations at $\boldsymbol{Q} = (3-q, \pm(3+q), 0)$.

doped materials, except for mode 2 (see Fig.5.2 (d) and Fig.5.3 (d)). The discrepancy between the calculated dispersion for mode 2 and the experimental values might be an indication of some missing ingredient that is not properly included in the calculations (e.g. orbital ordering). Nonetheless, the degree of agreement with the experimental data suggests that linear rescaling model in Eq. 5.1 is a good starting point to describe lattice dynamics of iron-pnictides.

5.1.2 Physical implications of the modified model

Having established the better overall agreement with the data, we now move on to the physical interpretation of our results. The lattice degree of freedom in iron-pnictides is intimately coupled to the spin degree of freedom through magneto-elastic coupling[90]. It is therefore useful to discuss the microscopic nature of magnetism and its possible effects on phonons.

The outstanding discrepancy between the measured and calculated phonon dispersion is that DFT calculation significantly overestimates the phonon anisotropy of parent $SrFe_2As_2$ over the entire Brillouin zone (although we note that a small anisotropy in doped material is a consequence of the suppression of the AFM order in underdoped regime). This is reminiscent of the tendency of DFT calculations to give a significantly larger ordered moment ($\sim 2\mu_B$/Fe) [45, 46] than is observed in most experiments ($\sim 0.9\mu_B$)[33, 34]. It is interesting to note that a reduction factor of $\lambda = 0.35$ in Eq. (5.1) relative to the DFT is roughly comparable to that found for magnetic moment. This suggests that the magnitude of mode splitting is proportional to the size of the ordered moments.

On the other hand, recent Fe $3s$ core level photoemission spectroscopy

has revealed the presence of large local moment of $\sim 2\mu_B$ fluctuating on a femtosecond time scale in the PM phase[146]. [2] These fluctuating local moments are expected to be ordered below T_N, but the size of the ordered moment is significantly smaller than that of the local moments above T_N, suggesting the presence of residual magnetic fluctuations persisting even in the AFM ordered phase. While the SDW picture for itinerant electrons with nested Fermi surface provides a reasonable framework to understand the AFM order in iron-pnictides, there are realistically some deviations from this simple physical picture [149]. The presence of large local moments at room temperature[146] is apparently incompatible with the SDW picture, where magnetic moments are formed simultaneously with the development of a static long-range magnetic order[149]. Thus, the magnetic state in iron-pnictides is not well described by either purely itinerant, or localized picture, but rather has a dual nature of the two.

On the theoretical side, there have been several attempts to understand the origin of the reduced ordered moment beyond DFT, using dynamical mean-field theory (DMFT) [147, 150, 151]. These can explain the presence of large local moments which only give rise to much smaller ordered moment below T_N. For example, Z. P. Yin *et al.* have suggested that there is the strong orbital differentiation, with the t_{2g} orbitals more correlated than the e_g

---

[2]The photoemission process allows for the detection of local magnetic moments fluctuating on extremely fast time scales characteristic of electron dynamics ($10^{-16} - 10^{-15}$ s), which cannot be measured by the conventional magnetic measurements such as nuclear magnetic resonance (NMR), Mössbauer spectroscopy and muon spin rotation (μSR) with typical probing time scales of $\sim 10^{-8}$ s or slower. The $\boldsymbol{q}$- and ω-integrated inelastic neutron scattering (INS) spectrum can, in principle, give access to the magnetic fluctuating on such a fast time scales, but in practice, the frequency range of typical INS experiments is usually limited up to ~ 300 meV (i.e. ~ 15 fs), which is still, at least, 1 or 2 orders of magnitude slower that short time scales typical of fast quantum fluctuations[147, 148]. Therefore, in most experiments, except for the case of photoemission spectroscopy, the magnetic moment represents the average over long time scales.
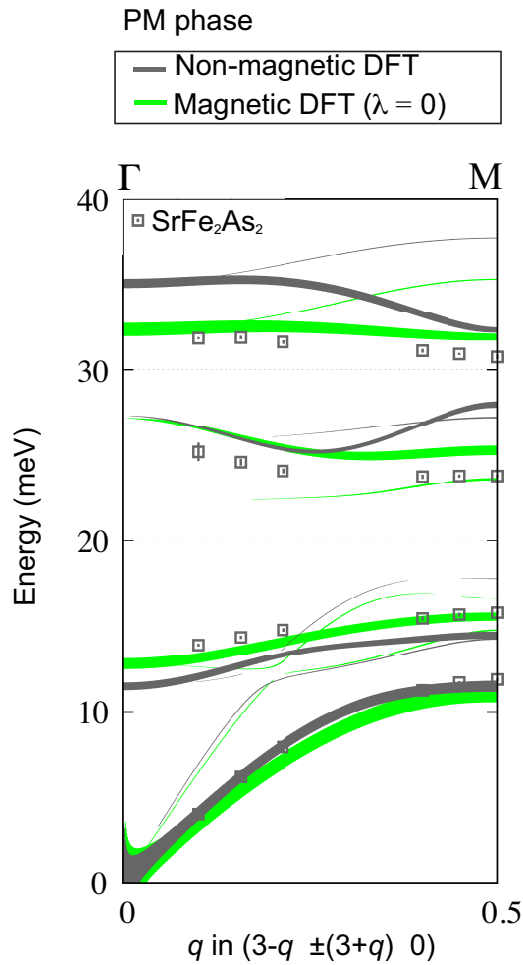
Figure 5.4: Comparison of the measured dispersion of $SrFe_2As_2$ in the PM phase and DFT calculations at $\boldsymbol{Q} = (3 - q, \pm(3 + q), 0)$. In both DFT calculations, two $\Gamma - M$ directions are equivalent.

orbitals[151]. This is analogous to the orbital-selective Mott transition, where localized and itinerant electrons in different orbitals separate as independent degrees of freedom[152, 153]. In this situation, the static ordered moment originates predominantly from more localized t_{2g} orbitals while fluctuating local moments in the e_g orbitals do not acquire a static component below T_N. Such orbital-selective correlations result in the reduced ordered moment in the AFM phase, and in analogy to this, one can expect the reduced phonon anisotropy.

In this context, the C_2 term of Eq.(5.1) arises from the ordered moment while the C_4 term includes the contribution of the fluctuating moments. Note that even in the PM phase, where long-range AFM order is destroyed, the averaged magnetic FC matrices $\phi_{ld\alpha,l'd'\beta}^{C_4}$ ($\lambda = 0$ in Eq.5.1) gives better agreement with phonon dispersion than non-magnetic DFT (see grey and green curves in Fig.5.4). We take this as an indication of the presence of fluctuating magnetism above T_N, consistent with Ref. [146]. Thus, the model in Eq.5.1 serves as a general model of phonons in this material applicable to both the AFM ordered phase and the PM phase.

We note that recently it was found, for small $\boldsymbol{q}$, that TA modes polarized in the [1 0 0] direction soften at[99] and above[98] $T_{s,N}$, and this was suggested to be related to the size of the fluctuating magnetic domains[98]. While different than the present work, where we observe clear energy splitting over the full zone below $T_{s,N}$, for differently polarized modes, that work also shows the sensitivity of the phonon measurements to magnetic order, and, indeed serves to highlight the potential to use careful phonon measurements to investigate both static and dynamical aspects of magneto-elastic coupling.

5.2   Discussion on the fluctuation timescale

To understand the effect of fluctuations on the phonon response, we consider a simple model meant to confirm expectations for the important time scales for a vibrating system where there are fast fluctuations of the force constants[3]. We show that the relevant time scales are the mode splitting in the slow fluctuation limit, which we call s, and the mean time between fluctua-

---

[3]Main contents of this section can be found in Supplemental Material of Ref[154].

tions, τ. The frequency broadening introduced by the fluctuations differs in two regimes determined by $\tau s \ll 1$ and $\tau s \gg 1$. The average mode frequency does not enter the problem.

We consider a mass, m, on a Hook's law spring ($F = ma = -kx$) where the force constant, k, switches between different values, with the change assumed to be fast, and the dwell time for interval i with constant k_i, given by τ_i. Then on each time interval $(t_i, t_{i+1}) = (t_i, t_i + \tau_i)$ one has a simple harmonic response

$$x_i(t) = a_i \sin(\omega_i t + \phi_i) \quad (t_i < t < t_{i+1}), \tag{5.2}$$

where $\omega_i = \sqrt{k_i/m}$ and a_i, ϕ_i are given by boundary conditions. We are interested in the power spectrum of the system, $I(\omega) \equiv |\tilde{x}(\omega)|^2$, where $\tilde{x}(\omega)$ is Fourier transform of the position given by

$$
\begin{aligned}
\tilde{x}(\omega) &= \int_{-\infty}^{+\infty} e^{-i\omega t} x(t) dt = \sum_i a_i \int_{t_i}^{t_{i+1}} e^{-i\omega t} \sin(\omega_i t + \phi_i) dt \\
&= \sum_i \frac{a_i}{\omega^2 - \omega_i^2} \Big[e^{-i\omega t_{i+1}} \Big(\omega_i \cos(\omega_i t_{i+1} + \phi_i) + i\omega \sin(\omega_i t_{i+1} + \phi_i) \Big) \\
&\qquad\qquad - e^{-i\omega t_i} \Big(\omega_i \cos(\omega_i t_i + \phi_i) + i\omega \sin(\omega_i t_i + \phi_i) \Big) \Big]
\end{aligned}
$$

$$\tag{5.3}$$

We limit ourselves to switching between two values, $k_{2n+1} = k_1$ and $k_{2n} = k_2$ and assume $k_1 < k_2$, taking $\Omega = \omega_2 - \omega_1 = \sqrt{k_2/m} - \sqrt{k_1/m}$ and $s = \Omega/2\pi$. We assume the motion is continuous (there are no instantaneous translations of the mass) and has fixed amplitude $a_i = a \ \forall i$. The phases are then given by, $\phi_{i+1} = \phi_i + (\omega_i - \omega_{i+1})t_i$. We take the dwell times to be randomly distributed according to a negative exponential, with mean dwell time, τ , so that the
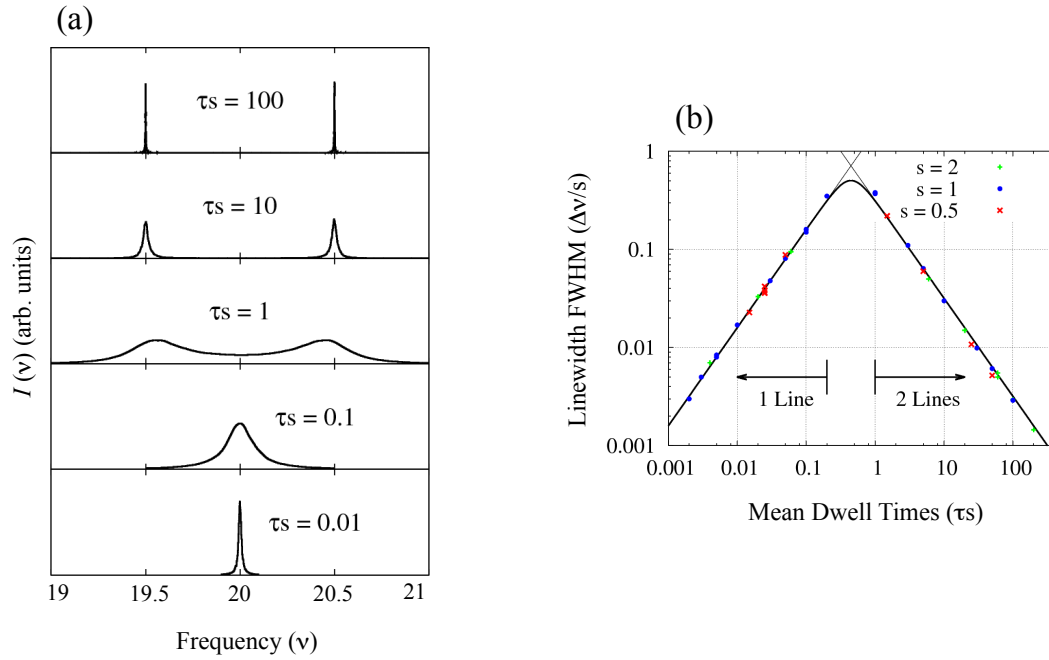
Figure 5.5: Effect of the fluctuations on the phonon response. (a) Power spectra for different dwell times. The line splitting s was set constant at 1 and the frequency scale has arbitrarily been centered at 20. (b) Normalized line width. The points are determined from the calculated power spectra with splitting, s as indicated. The solid lines are the formulas from the text.

probability of a particular dwell time is given by

$$P(\tau_i) = \frac{1}{\tau} e^{\frac{-\tau_i}{\tau}} \tag{5.4}$$

Attempts to find a general closed form solution were not successful, but the problem can be solved numerically by considering N intervals ($i = 1...N$), and letting N get large. In fact one has to be slightly careful, as the Fourier transform, in the usual way, will have fast oscillations (uninteresting noise) with a frequency scale given by $v_{osc} \sim (N\tau)^{-1}$ - one must insure that v_{osc} is small compared to any line width in the problem. This forces N to be fairly large when τ becomes small. We also assume a finite frequency resolution,

which also must be small compared to any interesting line width. Fig.5.5 (a) shows the power spectrum $I(\nu = \omega/2\pi)$ for several different values of the mean dwell time. The progression from two well separated lines for $\tau s \gg 1$ to a single collapsed line at the mean frequency for $\tau s \ll 1$ is clear, with a transition region with two broad overlapping peaks for $0.2 < \tau s < 1$. The line width, the full width at half maximum (FWHM), $\Delta\nu$ behaves differently in each region. Fitting the numerical results, for $\tau s \gg 1$ one finds each peak has a width $\Delta\nu \sim 1/(\pi\tau)$ while for $\tau s \ll 1$ the single peak is seen to have width approximately given by $\Delta\nu \sim \sqrt{8/\pi}\tau s^2$. A formula that gives a reasonable fit (except near $\tau s \sim 0.5$ where one has two highly-overlapping lines) is

$$\frac{\Delta\nu}{s} \sim \sqrt{\frac{8}{\pi}} \frac{\tau s}{\sqrt{1 + 8\pi\tau^4 s^4}} \tag{5.5}$$

As can be seen in Fig.5.5 (b), this gives a reasonable approximation at least for $0.002 < \tau s < 200$, $s = 0.5, 1$, and 2. We expect this to be valid over a larger range as well.

Taking, as an example, the phonon widths quoted earlier of $\Gamma_+ = 0.74 \pm 0.09$ meV above $T_{s,N}$ and $\Gamma_- = 0.70 \pm 0.10$ meV below $T_{s,N}$ with a splitting of $hs = 0.81$ meV, and assuming other contributions to the line width do not change through $T_{s,N}$, suggests a mean magnetic fluctuation frequency $1/\tau > 1.4$ THz. This assumes the broadening above $T_{s,N}$ is less than $0.04 + 0.14 = 0.18$ meV, where the 0.14 is the error on the difference. This frequency is lower than the limits suggested by other methods [146], but still valuable. A measurement with higher resolution (e.g. ~ 0.01 meV as has been demonstrated in Ref.[125]) might determine the fluctuation frequency more exactly.

Chapter 6

Concluding Remarks

The surprising discovery of superconductivity in iron-pnictides in 2008 [9] with T_c reaching 55 K has generated tremendous excitement in the field. Current understanding of iron-pnictide superconductors generally does not favor phonon-mediated pairing[68], but there remain outstanding puzzles regarding the phonon behavior in these materials. These include (1) a failure to observe the predicted phonon splitting in the AFM ordered phase, and (2) a tendency of magnetic DFT calculations to be better than non-magnetic ones for fitting the energies of some phonon modes, but to predict too large phonon splitting. Using state of the art IXS spectrometers at SPring-8 and phonon calculations, we were able to resolve these puzzles. Most significantly, our x-ray scattering measurements reveal the key role of the Fe-magnetism in the lattice dynamics of iron-pnictides. In the following, we summarize the main results and physical implication of our IXS studies.

1: Observation of mode splitting in the AFM phase

Although the existence of anisotropic behaviour, often referred to as nematic order, is now a well-established experimental fact in iron-pnictides,

the phonon response is surprisingly isotropic[95, 97]. In this thesis, we investigated temperature and doping dependence of phonon dispersion of detwinned single crystal of $Sr(Fe_{1-x}Co_x)_2As_2$ with $x = 0$, and 0.08. The importance of our results lies in the fact that we are able to observe clear anisotropy in phonon structure, and show that previous experiments have not seen such anisotropy due to the presence of twinning.

In the underdoped regime, 122 family of iron pnictides exhibits two phase transitions (e.g. orthorhombic structural distortion and the AFM phase transition), both of which can, in principle, give rise to C_4 to C_2 symmetry change in phonon dispersion. Our results, however, suggests that the orthorhombic distortion by itself is not sufficient to explain the phonon changes at low temperatures, and therefore the observed anisotropy is predominantly the result of the static AFM order that breaks the C_4 rotational symmetry of the underlying crystalline lattice.

2: Comparison with DFT calculations

To gain insight into our results, we compared our IXS data to DFT calculations. Magnetic DFT calculations give better agreement than non-magnetic DFT calculations, but in most parts of the Brillouin zone investigated, they significantly overestimate the magnitude of the mode splitting. We model the observed phonon anisotropy using magnetic DFT calculations, including a phenomenological reduction in force-constant anisotropy in a way that fits best to the observed mode splitting. We find good agreement with the data when a reduction factor for force constant anisotropy relative to the original DFT is roughly comparable to that found for magnetic moment. In analogy to the small ordered moment

in iron-pnictides, we suggest that the presence of magnetic fluctuations significantly reduces the phonon anisotropy that reflects the coupling to the static magnetic order. This is consistent with recent DMFT calculations of Refs[150, 151], which suggests the presence of residual magnetic fluctuations persisting in the AFM ordered state. As an important consequence of this interpretation, phonon dispersion is shown to be in good agreement with the magnetic-DFT calculation even in the PM phase, due to the fluctuating local moments[146] above T_N. Thus, this modified model serves as a starting point for a general model of phonons in iron-pnictide materials applicable to both the AFM ordered phase and the PM phase. This work highlights the potential to use careful phonon measurements as a probe of magnetism and its microscopic origin in iron-pnictide materials.

3: Future work

The present results provides substantial insight into understanding both static and dynamical aspects of magneto-elastic coupling in iron-pnictides, which could lead to better understanding of the underlying mechanism of superconductivity. Future work might be expected in several directions. Of particular interest is to extend the present work to the superconducting regime. Given the strong sensitivity of the superconductivity to the lattice geometry[87, 88, 89] together with the involvement of spin fluctuations in the pairing mechanism of iron-pnictides[69, 70], there may be an as yet unexplored aspect of magneto-elastic coupling related to the superconductivity. If this is indeed the case, it would be interesting to revisit superconducting iron pnictide materials. In particular recent

neutron diffraction study on hole-doped $Ba_{1-x}Na_xFe_2As_2$ has shown the phase competition between lattice, magnetism and superconductivity[155], which appears to be a worthwhile target for future systematic studies. We note that FeSe is of particular interest with respect to the relation between lattice and superconductivity due to the absence of the AFM order at ambient pressure [40].

Appendix A

Lattice dynamics and atomic force constants

The standard formalism for lattice dynamics is summarized. The dynamical matrix is introduced, and it is shown that phonon frequencies are obtained by the eigenvalue problem of the dynamical matrix and that atomic motions are given by the eigenvectors.

In the Born-Oppenheimer (adiabatic) approximation, the nuclear motion is determined by the Hamiltonian H

$$H = \frac{1}{2} \sum_{ld\alpha} M_d \dot{u}_{ld\alpha} + \frac{1}{2} \sum_{ld\alpha, l'd'\beta} \phi_{ld\alpha, l'd'\beta} u_{ld\alpha} u_{l'd'\beta} \quad , \tag{A.1}$$

where $u_{ld\alpha}$ denotes the displacement of atom d in unit cell l, α, β are the cartesian directions, and the coefficient $\phi_{ld\alpha, l'd'\beta}$ is called interatomic force constant matrix, which links atomic displacements $u_{l'd'\beta}$ to the force $F_{ld\alpha}$ on

the atom as

$$F_{ld\alpha} = -\sum_{l'd'\beta} \phi_{ld\alpha,l'd'\beta} u_{l'd'\beta} \ . \tag{A.2}$$

One should note that the $\phi_{ld\alpha,l'd'\beta}$ must obey the following symmetry relations

$$\sum_{l'd^7} \phi_{ld\alpha,l'd'\beta} = 0 \ . \tag{A.3}$$

This is so-called acoustic sum rule, and is a consequence of translational invariance, specifically, the requirement that when the crystal is rigidly shifted, the force on each atom must be zero.

From A.2, one immediately obtains the equation of motion,

$$M_d \ddot{u}_{ld\alpha} = -\sum_{l'd'\beta} \phi_{ld\alpha,l'd'\beta} u_{l'd'\beta} \ . \tag{A.4}$$

Considering that the solutions of Eq.A.4 are of the form of a superposition of normal modes with frequency ω and wave vector $\boldsymbol{q}$, one can reduce Eq.A.4 to the following eigenvalue problem,

$$\sum_{d'\beta} D_{\boldsymbol{q},d\alpha,d'\beta} \ e_{\boldsymbol{q},d'\beta} = \omega_{\boldsymbol{q},j}^2 \ e_{\boldsymbol{q},d\alpha} \ , \tag{A.5}$$

where the $3n$ atomic displacement $e_{\boldsymbol{q},d\alpha}$ ($\alpha = 1, 2, 3$; $d = 1, 2, 3.....n$, n is the number of atoms in the primitive unit cell.) are the components of an eigenvector $\boldsymbol{e_q}$ of $\boldsymbol{D_q}$ which belong to the eigenvalue $\omega_{\boldsymbol{q},j}$ ($j = 1, 2, 3...3n$). The relation expressed by $\omega = \omega_{\boldsymbol{q},j}$ is known as dispersion relation of phonon. The dynamical matrix $\boldsymbol{D_q}$ is composed of an $n \times n$ array of small 3×3 matrices.

The elements of the small 3×3 blocks of the dynamical matrix are given as

$$D_{\boldsymbol{q},d\alpha,d'\beta} = \frac{1}{\sqrt{M_d M_{d'}}} \sum_{l'} \phi_{ld\alpha,l'd'\beta} \exp\{i\boldsymbol{q} \cdot (\boldsymbol{r}_{l'd'} - \boldsymbol{r}_{ld})\} \quad . \tag{A.6}$$

One notes that the dynamical matrix $\boldsymbol{D_q}$ is Hermitian, and therefore eigenvalues $\omega^2_{\boldsymbol{q},j}$ are real.

Bibliography

[1] J. Bardeen, L. N. Cooper, and J. R. Schrieffer, Phys. Rev. **108**, 1175 (1957).

[2] A. P. Drozdov, M. I. Eremets, I. A. Troyan, V. Ksenofontov, and S. I. Shylin, Nature **525**, 73 (2015).

[3] V. Ginzburg and D. Kirzhnits, Physics Reports **4**, 343 (1972).

[4] J. R. Gavaler, Applied Physics Letters **23** (1973).

[5] J. Bednorz and K. A. Müller, Zeitschrift fr Physik B Condensed Matter **64**, 189 (1986).

[6] A. Schilling, M. Cantoni, J. D. Guo, and H. R. Ott, Nature **363**, 56 (1993).

[7] L. Gao, Y. Y. Xue, F. Chen, Q. Xiong, R. L. Meng, D. Ramirez, C. W. Chu, J. H. Eggert, and H. K. Mao, Phys. Rev. B **50**, 4260 (1994).

[8] P. A. Lee, N. Nagaosa, and X.-G. Wen, Rev. Mod. Phys. **78**, 17 (2006).

[9] Y. Kamihara, M. Hirano, and H. Hosono, J. Am. Chem. Soc **130**, 3296 (2008).

[10] Z.-A. Ren, G.-C. Che, X.-L. Dong, J. Yang, W. Lu, W. Yi, X.-L. Shen, Z.-C. Li, L.-L. Sun, F. Zhou, and Z.-X. Zhao, EPL (Europhysics Letters) **83**, 17002 (2008).

[11] G. F. Chen, Z. Li, D. Wu, G. Li, W. Z. Hu, J. Dong, P. Zheng, J. L. Luo, and N. L. Wang, Phys. Rev. Lett. **100**, 247002 (2008).

[12] R. Zhi-An, L. Wei, Y. Jie, Y. Wei, S. Xiao-Li, Zheng-Cai, C. Guang-Can, D. Xiao-Li, S. Li-Ling, Z. Fang, and Z. Zhong-Xian, Chinese Physics Letters **25**, 2215 (2008).

[13] S. Avci, O. Chmaissem, E. A. Goremychkin, S. Rosenkranz, J.-P. Castellan, D. Y. Chung, I. S. Todorov, J. A. Schlueter, H. Claus, M. G. Kanatzidis, A. Daoud-Aladine, D. Khalyavin, and R. Osborn, Phys. Rev. B **83**, 172503 (2011).

[14] H. Chen, Y. Ren, Y. Qiu, W. Bao, R. H. Liu, G. Wu, T. Wu, Y. L. Xie, X. F. Wang, Q. Huang, and X. H. Chen, EPL (Europhysics Letters) **85**, 17006 (2009).

[15] S. Aswartham, M. Abdel-Hafiez, D. Bombor, M. Kumar, A. U. B. Wolter, C. Hess, D. V. Evtushinsky, V. B. Zabolotnyy, A. A. Kordyuk, T. K. Kim, S. V. Borisenko, G. Behr, B. Büchner, and S. Wurmehl, Phys. Rev. B **85**, 224520 (2012).

[16] J.-H. Chu, J. G. Analytis, K. De Greve, P. L. McMahon, Z. Islam, Y. Yamamoto, and I. R. Fisher, Science **329**, 824 (2010).

[17] S. Nandi, M. G. Kim, A. Kreyssig, R. M. Fernandes, D. K. Pratt, A. Thaler, N. Ni, S. L. Bud'ko, P. C. Canfield, J. Schmalian, R. J. McQueeney, and A. I. Goldman, Phys. Rev. Lett. **104**, 057006 (2010).

[18] L. J. Li, Y. K. Luo, Q. B. Wang, H. Chen, Z. Ren, Q. Tao, Y. K. Li, X. Lin, M. He, Z. W. Zhu, G. H. Cao, and Z. A. Xu, New Journal of Physics **11**, 025008 (2009).

[19] P. C. Canfield, S. L. Bud'ko, N. Ni, J. Q. Yan, and A. Kracher, Phys. Rev. B **80**, 060501 (2009).

[20] S. Jiang, H. Xing, G. Xuan, C. Wang, Z. Ren, C. Feng, J. Dai, Z. Xu, and G. Cao, Journal of Physics: Condensed Matter **21**, 382203 (2009).

[21] S. Kasahara, T. Shibauchi, K. Hashimoto, K. Ikada, S. Tonegawa, R. Okazaki, H. Shishido, H. Ikeda, H. Takeya, K. Hirata, T. Terashima, and Y. Matsuda, Phys. Rev. B **81**, 184519 (2010).

[22] C. de la Cruz, Q. Huang, J. W. Lynn, J. Li, W. R. II, J. L. Zarestky, H. A. Mook, G. F. Chen, J. L. Luo, N. L. Wang, and P. Dai, Nature **453**, 899 (2008).

[23] Q. Huang, J. Zhao, J. W. Lynn, G. F. Chen, J. L. Luo, N. L. Wang, and P. Dai, Phys. Rev. B **78**, 054529 (2008).

[24] J. Zhao, Q. Huang, C. de la Cruz, S. Li, J. W. Lynn, Y. Chen, M. A. Green, G. F. Chen, G. Li, Z. Li, J. L. Luo, N. L. Wang, and P. Dai, Nat Mater **7**, 953 (2008).

[25] S. A. J. Kimber, D. N. Argyriou, F. Yokaichiya, K. Habicht, S. Gerischer, T. Hansen, T. Chatterji, R. Klingeler, C. Hess, G. Behr, A. Kondrat, and B. Büchner, Phys. Rev. B **78**, 140503 (2008).

[26] Y. Chen, J. W. Lynn, J. Li, G. Li, G. F. Chen, J. L. Luo, N. L. Wang, P. Dai, C. dela Cruz, and H. A. Mook, Phys. Rev. B **78**, 064515 (2008).

[27] Y. Qiu, W. Bao, Q. Huang, T. Yildirim, J. M. Simmons, M. A. Green, J. W. Lynn, Y. C. Gasparovic, J. Li, T. Wu, G. Wu, and X. H. Chen, Phys. Rev. Lett. **101**, 257002 (2008).

[28] A. I. Goldman, D. N. Argyriou, B. Ouladdiaf, T. Chatterji, A. Kreyssig, S. Nandi, N. Ni, S. L. Bud'ko, P. C. Canfield, and R. J. McQueeney, Phys. Rev. B **78**, 100506 (2008).

[29] A. I. Goldman, A. Kreyssig, K. Prokeš, D. K. Pratt, D. N. Argyriou, J. W. Lynn, S. Nandi, S. A. J. Kimber, Y. Chen, Y. B. Lee, G. Samolyuk, J. B. Leão, S. J. Poulton, S. L. Bud'ko, N. Ni, P. C. Canfield, B. N. Harmon, and R. J. McQueeney, Phys. Rev. B **79**, 024513 (2009).

[30] A. Kreyssig, M. A. Green, Y. Lee, G. D. Samolyuk, P. Zajdel, J. W. Lynn, S. L. Bud'ko, M. S. Torikachvili, N. Ni, S. Nandi, J. B. Leão, S. J. Poulton, D. N. Argyriou, B. N. Harmon, R. J. McQueeney, P. C. Canfield, and A. I. Goldman, Phys. Rev. B **78**, 184517 (2008).

[31] A. Jesche, N. Caroca-Canales, H. Rosner, H. Borrmann, A. Ormeci, D. Kasinathan, H. H. Klauss, H. Luetkens, R. Khasanov, A. Amato, A. Hoser, K. Kaneko, C. Krellner, and C. Geibel, Phys. Rev. B **78**, 180504 (2008).

[32] K. Kaneko, A. Hoser, N. Caroca-Canales, A. Jesche, C. Krellner, O. Stockert, and C. Geibel, Phys. Rev. B **78**, 212502 (2008).

[33] J. Zhao, W. Ratcliff, J. W. Lynn, G. F. Chen, J. L. Luo, N. L. Wang, J. Hu, and P. Dai, Phys. Rev. B **78**, 140504 (2008).

[34] Q. Huang, Y. Qiu, W. Bao, M. A. Green, J. W. Lynn, Y. C. Gasparovic, T. Wu, G. Wu, and X. H. Chen, Phys. Rev. Lett. **101**, 257003 (2008).

[35] M. G. Kim, D. K. Pratt, G. E. Rustan, W. Tian, J. L. Zarestky, A. Thaler, S. L. Bud'ko, P. C. Canfield, R. J. McQueeney, A. Kreyssig, and A. I. Goldman, Phys. Rev. B **83**, 054514 (2011).

[36] S. Li, C. de la Cruz, Q. Huang, G. F. Chen, T.-L. Xia, J. L. Luo, N. L. Wang, and P. Dai, Phys. Rev. B **80**, 020504 (2009).

[37] J. H. Tapp, Z. Tang, B. Lv, K. Sasmal, B. Lorenz, P. C. W. Chu, and A. M. Guloy, Phys. Rev. B **78**, 060505 (2008).

[38] M. J. Pitcher, D. R. Parker, P. Adamson, S. J. C. Herkelrath, A. T. Boothroyd, R. M. Ibberson, M. Brunelli, and S. J. Clarke, Chem. Commun. , 5918 (2008).

[39] F.-C. Hsu, J.-Y. Luo, K.-W. Yeh, T.-K. Chen, T.-W. Huang, P. M. Wu, Y.-C. Lee, Y.-L. Huang, Y.-Y. Chu, D.-C. Yan, and M.-K. Wu, Proceedings of the National Academy of Sciences **105**, 14262 (2008).

[40] A. E. Böhmer, F. Hardy, F. Eilers, D. Ernst, P. Adelmann, P. Schweiss, T. Wolf, and C. Meingast, Phys. Rev. B **87**, 180505 (2013).

[41] J. T. Greenfield, S. Kamali, K. Lee, and K. Kovnir, Chemistry of Materials **27**, 588 (2015).

[42] K.-W. Yeh, T.-W. Huang, Y. lin Huang, T.-K. Chen, F.-C. Hsu, P. M. Wu, Y.-C. Lee, Y.-Y. Chu, C.-L. Chen, J.-Y. Luo, D.-C. Yan, and M.-K. Wu, EPL (Europhysics Letters) **84**, 37002 (2008).

[43] M. H. Fang, H. M. Pham, B. Qian, T. J. Liu, E. K. Vehstedt, Y. Liu, L. Spinu, and Z. Q. Mao, Phys. Rev. B **78**, 224503 (2008).

[44] S. Medvedev, T. M. McQueen, I. A. Troyan, T. Palasyuk, M. I. Eremets, R. J. Cava, S. Naghavi, F. Casper, V. Ksenofontov, G. Wortmann, and C. Felser, Nat Mater **8**, 630 (2009).

[45] I. I. Mazin, M. D. Johannes, L. Boeri, K. Koepernik, and D. J. Singh, Phys. Rev. B **78**, 085104 (2008).

[46] I. I. Mazin and M. D. Johannes, Nat Phys **5**, 141 (2009).

[47] T. Yildirim, Phys. Rev. Lett. **101**, 057010 (2008).

[48] J.-H. Chu, J. G. Analytis, C. Kucharczyk, and I. R. Fisher, Phys. Rev. B **79**, 014506 (2009).

[49] C. Lester, J.-H. Chu, J. G. Analytis, S. C. Capelli, A. S. Erickson, C. L. Condron, M. F. Toney, I. R. Fisher, and S. M. Hayden, Phys. Rev. B **79**, 144523 (2009).

[50] D. K. Pratt, W. Tian, A. Kreyssig, J. L. Zarestky, S. Nandi, N. Ni, S. L. Bud'ko, P. C. Canfield, A. I. Goldman, and R. J. McQueeney, Phys. Rev. Lett. **103**, 087001 (2009).

[51] M. Wang, H. Luo, J. Zhao, C. Zhang, M. Wang, K. Marty, S. Chi, J. W. Lynn, A. Schneidewind, S. Li, and P. Dai, Phys. Rev. B **81**, 174524 (2010).

[52] A. J. Drew, C. Niedermayer, P. J. Baker, F. L. Pratt, S. J. Blundell, T. Lancaster, R. H. Liu, G. Wu, X. H. Chen, I. Watanabe, V. K. Malik, A. Dubroka, M. Rossle, K. W. Kim, C. Baines, and C. Bernhard, Nat Mater **8**, 310 (2009).

[53] H. Luetkens, H. H. Klauss, M. Kraken, F. J. Litterst, T. Dellmann, R. Klingeler, C. Hess, R. Khasanov, A. Amato, C. Baines, M. Kosmala, O. J. Schumann, M. Braden, J. Hamann-Borrero, N. Leps, A. Kondrat, G. Behr, J. Werner, and B. Buchner, Nat Mater **8**, 305 (2009).

[54] J. Zhao, Q. Huang, C. de la Cruz, S. Li, J. W. Lynn, Y. Chen, M. A. Green, G. F. Chen, G. Li, Z. Li, J. L. Luo, N. L. Wang, and P. Dai, Nat Mater **7**, 953 (2008).

[55] F. C. Zhang and T. M. Rice, Phys. Rev. B **37**, 3759 (1988).

[56] D. J. Singh and M.-H. Du, Phys. Rev. Lett. **100**, 237003 (2008).

[57] D. Singh, Physica C: Superconductivity **469**, 418 (2009), superconductivity in Iron-Pnictides.

[58] K. Nakamura, R. Arita, and M. Imada, Journal of the Physical Society of Japan **77**, 093711 (2008).

[59] I. Mazin and J. Schmalian, Physica C: Superconductivity **469**, 614 (2009), superconductivity in Iron-Pnictides.

[60] H. Ding, P. Richard, K. Nakayama, K. Sugawara, T. Arakane, Y. Sekiba, A. Takayama, S. Souma, T. Sato, T. Takahashi, Z. Wang, X. Dai, Z. Fang, G. F. Chen, J. L. Luo, and N. L. Wang, EPL (Europhysics Letters) **83**, 47001 (2008).

[61] T. Kondo, A. F. Santander-Syro, O. Copie, C. Liu, M. E. Tillman, E. D. Mun, J. Schmalian, S. L. Bud'ko, M. A. Tanatar, P. C. Canfield, and A. Kaminski, Phys. Rev. Lett. **101**, 147003 (2008).

[62] W. Malaeb, T. Yoshida, A. Fujimori, M. Kubota, K. Ono, K. Kihou, P. M. Shirage, H. Kito, A. Iyo, H. Eisaki, Y. Nakajima, T. Tamegai, and R. Arita, Journal of the Physical Society of Japan **78**, 123706 (2009).

[63] C. Liu, T. Kondo, N. Ni, A. D. Palczewski, A. Bostwick, G. D. Samolyuk, R. Khasanov, M. Shi, E. Rotenberg, S. L. Bud'ko, P. C. Canfield, and A. Kaminski, Phys. Rev. Lett. **102**, 167004 (2009).

[64] T. Yoshida, I. Nishi, S. Ideta, A. Fujimori, M. Kubota, K. Ono, S. Kasahara, T. Shibauchi, T. Terashima, Y. Matsuda, H. Ikeda, and R. Arita, Phys. Rev. Lett. **106**, 117001 (2011).

[65] T. Terashima, N. Kurita, M. Tomita, K. Kihou, C.-H. Lee, Y. Tomioka, T. Ito, A. Iyo, H. Eisaki, T. Liang, M. Nakajima, S. Ishida, S.-i. Uchida, H. Harima, and S. Uji, Phys. Rev. Lett. **107**, 176402 (2011).

[66] J. G. Analytis, R. D. McDonald, J.-H. Chu, S. C. Riggs, A. F. Bangura, C. Kucharczyk, M. Johannes, and I. R. Fisher, Phys. Rev. B **80**, 064507 (2009).

[67] K. Terashima, Y. Sekiba, J. H. Bowen, K. Nakayama, T. Kawahara, T. Sato, P. Richard, Y.-M. Xu, L. J. Li, G. H. Cao, Z.-A. Xu, H. Ding, and T. Takahashi, Proceedings of the National Academy of Sciences **106**, 7330 (2009).

[68] L. Boeri, O. V. Dolgov, and A. A. Golubov, Phys. Rev. Lett. **101**, 026403 (2008).

[69] K. Kuroki, S. Onari, R. Arita, H. Usui, Y. Tanaka, H. Kontani, and H. Aoki, Phys. Rev. Lett. **101**, 087004 (2008).

[70] I. I. Mazin, D. J. Singh, M. D. Johannes, and M. H. Du, Phys. Rev. Lett. **101**, 057003 (2008).

[71] T. Hanaguri, S. Niitaka, K. Kuroki, and H. Takagi, Science **328**, 474 (2010).

[72] S. A. Kivelson, E. Fradkin, and V. J. Emery, Nature **393**, 550 (1998).

[73] Y. Ando, K. Segawa, S. Komiya, and A. N. Lavrov, Phys. Rev. Lett. **88**, 137005 (2002).

[74] V. Hinkov, D. Haug, B. Fauqu, P. Bourges, Y. Sidis, A. Ivanov, C. Bernhard, C. T. Lin, and B. Keimer, Science **319**, 597 (2008).

[75] R. Daou, J. Chang, D. LeBoeuf, O. Cyr-Choiniere, F. Laliberte, N. Doiron-Leyraud, B. J. Ramshaw, R. Liang, D. A. Bonn, W. N. Hardy, and L. Taillefer, Nature **463**, 519 (2010).

[76] C.-C. Lee, W.-G. Yin, and W. Ku, Phys. Rev. Lett. **103**, 267001 (2009).

[77] W. Lv, J. Wu, and P. Phillips, Phys. Rev. B **80**, 224506 (2009).

[78] C. Fang, H. Yao, W.-F. Tsai, J. Hu, and S. A. Kivelson, Phys. Rev. B **77**, 224509 (2008).

[79] R. M. Fernandes, A. V. Chubukov, J. Knolle, I. Eremin, and J. Schmalian, Phys. Rev. B **85**, 024534 (2012).

[80] R. M. Fernandes, A. V. Chubukov, and J. Schmalian, Nat.Phys **10**, 97 (2014).

[81] S. Ishida, M. Nakajima, T. Liang, K. Kihou, C. H. Lee, A. Iyo, H. Eisaki, T. Kakeshita, Y. Tomioka, T. Ito, and S. Uchida, Phys. Rev. Lett. **110**, 207001 (2013).

[82] M. Nakajima, T. Liang, S. Ishida, Y. Tomioka, K. Kihou, C. H. Lee, A. Iyo, H. Eisaki, T. Kakeshita, T. Ito, and S. Uchida, Proc. Natl Acad. Sci USA **108**, 12238 (2011).

[83] M. Yi, D. Lu, J.-H. Chu, J. G. Analytis, A. P. Sorini, A. F. Kemper, B. Moritz, S.-K. Mo, R. G. Moore, M. Hashimoto, W.-S. Lee, Z. Hussain, T. P. Devereaux, I. R. Fisher, and Z.-X. Shen, Proc. Natl Acad. Sci USA **108**, 6878 (2011).

[84] Y. Zhang, C. He, Z. R. Ye, J. Jiang, F. Chen, M. Xu, Q. Q. Ge, B. P. Xie, J. Wei, M. Aeschlimann, X. Y. Cui, M. Shi, J. P. Hu, and D. L. Feng, Phys. Rev. B **85**, 085121 (2012).

[85] T. Shimojima, K. Ishizaka, Y. Ishida, N. Katayama, K. Ohgushi, T. Kiss, M. Okawa, T. Togashi, X.-Y. Wang, C.-T. Chen, S. Watanabe, R. Kadota, T. Oguchi, A. Chainani, and S. Shin, Phys. Rev. Lett. **104**, 057002 (2010).

[86] S. Kasahara, H. J. Shi, K. Hashimoto, S. Tonegawa, Y. Mizukami, T. Shibauchi, K. Sugimoto, T. Fukuda, T. Terashima, A. H. Nevidomskyy, and Y. Matsuda, Nature **486**, 382 (2012).

[87] C.-H. Lee, A. Iyo, H. Eisaki, H. Kito, M. Teresa Fernandez-Diaz, T. Ito, K. Kihou, H. Matsuhata, M. Braden, and K. Yamada, *Journal of the Physical Society of Japan*, Journal of the Physical Society of Japan **77**, 083704 (2008).

[88] Y. Mizuguchi, Y. Hara, K. Deguchi, S. Tsuda, T. Yamaguchi, K. Takeda, H. Kotegawa, H. Tou, and Y. Takano, Superconductor Science and Technology **23**, 054013 (2010).

[89] K. Kuroki, H. Usui, S. Onari, R. Arita, and H. Aoki, Phys. Rev. B **79**, 224511 (2009).

[90] T. Yildirim, Physica C: Superconductivity **469**, 425 (2009).

[91] T. Fukuda, A. Q. R. Baron, S. ichi Shamoto, M. Ishikado, H. Nakamura, M. Machida, H. Uchiyama, S. Tsutsui, A. Iyo, H. Kito, J. Mizuki, M. Arai, H. Eisaki, and H. Hosono, Journal of the Physical Society of Japan **77**, 103715 (2008).

[92] A. D. Christianson, M. D. Lumsden, O. Delaire, M. B. Stone, D. L. Abernathy, M. A. McGuire, A. S. Sefat, R. Jin, B. C. Sales, D. Mandrus, E. D. Mun, P. C. Canfield, J. Y. Y. Lin, M. Lucas, M. Kresch, J. B. Keith, B. Fultz, E. A. Goremychkin, and R. J. McQueeney, Phys. Rev. Lett. **101**, 157004 (2008).

[93] Y. Qiu, M. Kofu, W. Bao, S.-H. Lee, Q. Huang, T. Yildirim, J. R. D. Copley, J. W. Lynn, T. Wu, G. Wu, and X. H. Chen, Phys. Rev. B **78**, 052508 (2008).

[94] S. E. Hahn, G. S. Tucker, J.-Q. Yan, A. H. Said, B. M. Leu, R. W. McCallum, E. E. Alp, T. A. Lograsso, R. J. McQueeney, and B. N. Harmon, Phys. Rev. B **87**, 104518 (2013).

[95] T. Fukuda, A. Q. R. Baron, H. Nakamura, S. Shamoto, M. Ishikado, M. Machida, H. Uchiyama, A. Iyo, H. Kito, J. Mizuki, M. Arai, and H. Eisaki, Phys. Rev. B **84**, 064504 (2011).

[96] M. Le Tacon, T. R. Forrest, C. Rüegg, A. Bosak, A. C. Walters, R. Mittal, H. M. Rønnow, N. D. Zhigadlo, S. Katrych, J. Karpinski, J. P. Hill, M. Krisch, and D. F. McMorrow, Phys. Rev. B **80**, 220504 (2009).

[97] D. Reznik, K. Lokshin, D. C. Mitchell, D. Parshall, W. Dmowski, D. Lamago, R. Heid, K.-P. Bohnen, A. S. Sefat, M. A. McGuire, B. C. Sales, D. G. Mandrus, A. Subedi, D. J. Singh, A. Alatas, M. H. Upton, A. H. Said, A. Cunsolo, Y. Shvyd'ko, and T. Egami, Phys. Rev. B **80**, 214534 (2009).

[98] D. Parshall, L. Pintschovius, J. L. Niedziela, J.-P. Castellan, D. Lamago, R. Mittal, T. Wolf, and D. Reznik, Phys. Rev. B **91**, 134426 (2015).

[99] J. L. Niedziela, D. Parshall, K. A. Lokshin, A. S. Sefat, A. Alatas, and T. Egami, Phys. Rev. B **84**, 224305 (2011).

[100] C.-H. Lee, K. Kihou, K. Horigane, S. Tsutsui, T. Fukuda, H. Eisaki, A. Iyo, H. Yamaguchi, A. Q. R. Baron, M. Braden, and K. Yamada, Journal of the Physical Society of Japan **79**, 014714 (2010).

[101] R. Mittal, Y. Su, S. Rols, T. Chatterji, S. L. Chaplot, H. Schober, M. Rotter, D. Johrendt, and T. Brueckel, Phys. Rev. B **78**, 104514 (2008).

[102] D. Parshall, R. Heid, J. L. Niedziela, T. Wolf, M. B. Stone, D. L. Abernathy, and D. Reznik, Phys. Rev. B **89**, 064310 (2014).

[103] R. Mittal, L. Pintschovius, D. Lamago, R. Heid, K.-P. Bohnen, D. Reznik, S. L. Chaplot, Y. Su, N. Kumar, S. K. Dhar, A. Thamizhavel, and T. Brueckel, Phys. Rev. Lett. **102**, 217001 (2009).

[104] S. E. Hahn, Y. Lee, N. Ni, P. C. Canfield, A. I. Goldman, R. J. Mc-Queeney, B. N. Harmon, A. Alatas, B. M. Leu, E. E. Alp, D. Y. Chung, I. S. Todorov, and M. G. Kanatzidis, Phys. Rev. B **79**, 220511 (2009).

[105] D. Phelan, J. N. Millican, E. L. Thomas, J. B. Leão, Y. Qiu, and R. Paul, Phys. Rev. B **79**, 014519 (2009).

[106] L. Chauvière, Y. Gallais, M. Cazayous, A. Sacuto, M. A. Méasson, D. Colson, and A. Forget, Phys. Rev. B **80**, 094504 (2009).

[107] D. Reznik, L. Pintschovius, M. Ito, S. Iikubo, M. Sato, H. Goka, M. Fujita, K. Yamada, G. D. Gu, and J. M. Tranquada, Nature **440**, 1170 (2006).

[108] M. Le Tacon, A. Bosak, S. M. Souliou, G. Dellea, T. Loew, R. Heid, K.-P. Bohnen, G. Ghiringhelli, M. Krisch, and B. Keimer, Nat Phys **10**, 52 (2014).

[109] A. Q. Baron, J. P. Sutter, S. Tsutsui, H. Uchiyama, T. Masui, S. Tajima, R. Heid, and K.-P. Bohnen, Journal of Physics and Chemistry of Solids **69**, 3100 (2008).

[110] A. Q. R. Baron, ArXiv e-prints (2015), arXiv:1504.01098 [cond-mat.mtrl-sci] .

[111] A. Q. R. Baron, ArXiv e-prints (2009), arXiv:0910.5764 [cond-mat.mtrl-sci] .

[112] C. B. Walker, Phys. Rev. **103**, 547 (1956).

[113] B. N. Brockhouse and A. T. Stewart, Rev. Mod. Phys. **30**, 236 (1958).

[114] E. Burkel, J. Peisl, and B. Dorner, EPL (Europhysics Letters) **3**, 957 (1987).

[115] F. Sette, G. Ruocco, M. Krisch, U. Bergmann, C. Masciovecchio, V. Mazzacurati, G. Signorelli, and R. Verbeni, Phys. Rev. Lett. **75**, 850 (1995).

[116] A. Q. R. Baron, H. Uchiyama, Y. Tanaka, S. Tsutsui, D. Ishikawa, S. Lee, R. Heid, K.-P. Bohnen, S. Tajima, and T. Ishikawa, Phys. Rev. Lett. **92**, 197004 (2004).

[117] A. Q. R. Baron, H. Uchiyama, R. Heid, K. P. Bohnen, Y. Tanaka, S. Tsutsui, D. Ishikawa, S. Lee, and S. Tajima, Phys. Rev. B **75**, 020505 (2007).

[118] A. Shukla, M. Calandra, M. d'Astuto, M. Lazzeri, F. Mauri, C. Bellin, M. Krisch, J. Karpinski, S. M. Kazakov, J. Jun, D. Daghero, and K. Parlinski, Phys. Rev. Lett. **90**, 095506 (2003).

[119] Y. Nakajima, S. Imada, K. Hirose, T. Komabayashi, H. Ozawa, S. Tateno, S. Tsutsui, Y. Kuwayama, and A. Q. R. Baron, Nat Commun **6** (2015).

[120] F. Sette, M. H. Krisch, C. Masciovecchio, G. Ruocco, and G. Monaco, Science **280**, 1550 (1998).

[121] D. Ishikawa, M. Inui, K. Matsuda, K. Tamura, S. Tsutsui, and A. Q. R. Baron, Phys. Rev. Lett. **93**, 097801 (2004).

[122] K. Shibata, N. Takahashi, Y. Kawakita, M. Matsuura, T. Yamada, T. Tominaga, W. Kambara, M. Kobayashi, Y. Inamura, T. Nakatani, K. Nakajima, and M. Arai, JPS Conf. Proc. **8**, 036022 (2015).

[123] J. Wuttke, A. Budwig, M. Drochner, H. Kmmerling, F.-J. Kayser, H. Kleines, V. Ossovyi, L. C. Pardo, M. Prager, D. Richter, G. J. Schneider, H. Schneider, and S. Staringer, Review of Scientific Instruments **83**, 075109 (2012), 10.1063/1.4732806.

[124] T. Keller, K. Habicht, H. Klann, M. Ohl, H. Schneider, and B. Keimer, Applied Physics A **74**, s332 (2002).

[125] P. Aynajian, T. Keller, L. Boeri, S. M. Shapiro, K. Habicht, and B. Keimer, Science **319**, 1509 (2008).

[126] G. L. Squires, *Introduction to the theory of thermal neutron scattering* (Cambridge university press, 2012).

[127] E. Burkel, Springer Tracts in Modern Physics **125**, 1 (1991).

[128] E. Burkel, Reports on Progress in Physics **63**, 171 (2000).

[129] B. Fk and B. Dorner, Physica B: Condensed Matter **234236**, 1107 (1997), proceedings of the First European Conference on Neutron Scattering.

[130] A. Baron, Y. Tanaka, S. Goto, K. Takeshita, T. Matsushita, and T. Ishikawa, Journal of Physics and Chemistry of Solids **61**, 461 (2000).

[131] "Operating parameters of bl35xu," http://www.spring8.or.jp/wkg/BL35XU/instrument/lang-en/INS-0000001397/instrument_summary_view.

[132] A. Baron, SPring-8 Inf. Newsl, 2010 **15**, 14 (2010).

[133] F. James and M. Roos, Computer Physics Communications **10**, 343 (1975).

[134] T. Kobayashi, S. Miyasaka, S. Tajima, and N. Chikumoto, Journal of the Physical Society of Japan **83**, 104702 (2014).

[135] M. A. Tanatar, A. Kreyssig, S. Nandi, N. Ni, S. L. Bud'ko, P. C. Canfield, A. I. Goldman, and R. Prozorov, Phys. Rev. B **79**, 180508 (2009).

[136] E. C. Blomberg, M. A. Tanatar, A. Kreyssig, N. Ni, A. Thaler, R. Hu, S. L. Bud'ko, P. C. Canfield, A. I. Goldman, and R. Prozorov, Phys. Rev. B **83**, 134505 (2011).

[137] J.-H. Chu, J. G. Analytis, D. Press, K. De Greve, T. D. Ladd, Y. Yamamoto, and I. R. Fisher, Phys. Rev. B **81**, 214502 (2010).

[138] C. Dhital, Z. Yamani, W. Tian, J. Zeretsky, A. S. Sefat, Z. Wang, R. J. Birgeneau, and S. D. Wilson, Phys. Rev. Lett. **108**, 087001 (2012).

[139] Y. Song, S. V. Carr, X. Lu, C. Zhang, Z. C. Sims, N. F. Luttrell, S. Chi, Y. Zhao, J. W. Lynn, and P. Dai, Phys. Rev. B **87**, 184511 (2013).

[140] X. Lu, J. T. Park, R. Zhang, H. Luo, A. H. Nevidomskyy, Q. Si, and P. Dai, Science **345**, 657 (2014), http://science.sciencemag.org/content/345/6197/657.full.pdf .

[141] G. Kresse and J. Hafner, Phys. Rev. B **47**, 558 (1993).

[142] G. Kresse and J. Furthmller, Computational Materials Science **6**, 15 (1996).

[143] G. Kresse and J. Furthmüller, Phys. Rev. B **54**, 11169 (1996).

[144] K. Parlinski, Z. Q. Li, and Y. Kawazoe, Phys. Rev. Lett. **78**, 4063 (1997).

[145] F. Körmann, A. Dick, B. Grabowski, T. Hickel, and J. Neugebauer, Phys. Rev. B **85**, 125104 (2012).

[146] P. Vilmercati, A. Fedorov, F. Bondino, F. Offi, G. Panaccione, P. Lacovig, L. Simonelli, M. A. McGuire, A. S. M. Sefat, D. Mandrus, B. C. Sales, T. Egami, W. Ku, and N. Mannella, Phys. Rev. B **85**, 220503 (2012).

[147] P. Hansmann, R. Arita, A. Toschi, S. Sakai, G. Sangiovanni, and K. Held, Phys. Rev. Lett. **104**, 197002 (2010).

[148] A. Toschi, R. Arita, P. Hansmann, G. Sangiovanni, and K. Held, Phys. Rev. B **86**, 064411 (2012).

[149] P. Dai, J. Hu, and E. Dagotto, Nat Phys **8**, 709 (2012).

[150] Z. P. Yin, K. Haule, and G. Kotliar, Nat Phys **7**, 294 (2011).

[151] Z. P. Yin, K. Haule, and G. Kotliar, Nat Mater **10**, 932 (2011).

[152] V. Anisimov, I. Nekrasov, D. Kondakov, T. Rice, and M. Sigrist, The European Physical Journal B **25**, 191 (2002).

[153] A. Koga, N. Kawakami, T. M. Rice, and M. Sigrist, Phys. Rev. Lett. **92**, 216402 (2004).

[154] N. Murai, T. Fukuda, T. Kobayashi, M. Nakajima, H. Uchiyama, D. Ishikawa, S. Tsutsui, H. Nakamura, M. Machida, S. Miyasaka, S. Tajima, and A. Q. R. Baron, Phys. Rev. B **93**, 020301 (2016).

[155] S. Avci, O. Chmaissem, J. M. Allred, S. Rosenkranz, I. Eremin, A. V. Chubukov, D. E. Bugaris, D. Y. Chung, M. G. Kanatzidis, J. P. Castellan, J. A. Schlueter, H. Claus, D. D. Khalyavin, P. Manuel, A. Daoud-Aladine, and R. Osborn, Nat Commun **5** (2014).

List of Publication

Original papers

[1] N. Murai, T. Fukuda, T. Kobayashi, M. Nakajima, H. Uchiyama, D. Ishikawa, S. Tsutsui, H. Nakamura, M. Machida, S. Miyasaka, S. Tajima, and A. Q. R. Baron, **"Effect of magnetism on lattice dynamics in SrFe$_2$As$_2$ using high-resolution inelastic x-ray scattering"**, Phys. Rev. B **93**, 020301(R) (2016).

[2] N. Murai, T. Masui, M. Ishikado, S. Ishida, H. Eisaki, S. Uchida, and S. Tajima, **"Electronic Raman scattering on out-of-plane disordered Bi$_2$Sr$_2$CaCu$_2$O$_{8+\delta}$: How the pseudogap affects the superconducting Raman response"**, Phys. Rev. B **91**, 214520 (2015).

[3] N. Murai, T. Masui, M. Ishikado, S. Ishida, H. Eisaki, S. Uchida, and S. Tajima, **'"Effect of out-of-plane disorder on superconducting gap anisotropy in Bi$_{2+x}$Sr$_{2-x}$CaCu$_2$O$_{8+\delta}$ as seen via Raman spectroscopy"**, Phys. Rev. B **85**, 020507(R) (2012).

Proceedings

[1] N. Murai, T. Masui, M. Ishikado, S. Ishida, H. Eisaki, S. Uchida, and S. Tajima, **"Superconducting Gap Structure in Out-of-plane-disordered $Bi_2Sr_2CaCu_2O_{8+\delta}$ as Studied by Raman Spectroscopy"**, Procedia **45**, 37 (2013).

[2] N. Murai, T. Masui, M. Ishikado, S. Ishida, H. Eisaki, S. Uchida, and S. Tajima, **"Disorder-Induced Change of Gap Anisotropy in $Bi_{2+x}Sr_{2-x}CaCu_2O_{8+\delta}$ Studied by Raman Spectroscopy"**, Journal of the Physical Society of Japan **81**, SB033, (2012).

List of Conference

[1] N. Murai, T. Fukuda, T. Kobayashi, M. Nakajima, H. Uchiyama, D. Ishikawa, S. Tsutsui, H. Nakamura, M. Machida, S. Miyasaka, S. Tajima, and A. Q. R. Baron, **"Toward understanding phonons in magnetic and non-magnetic phases of $SrFe_2As_2$"**, Poster Presentation (N6)
The 9th International Conference on Inelastic X-ray Scattering, Hsinchu, Taiwan

[2] N. Murai, T. Fukuda, T. Kobayashi, M. Nakajima, H. Uchiyama, D. Ishikawa, S. Tsutsui, H. Nakamura, M. Machida, S. Miyasaka, S. Tajima, and A. Q. R. Baron, Oral Presentation (18pDB-14)
JPS, September 2015, Kansai University, Japan

[3] N. Murai, T. Fukuda, T. Kobayashi, M. Nakajima, H. Uchiyama, D. Ishikawa, S. Tsutsui, H. Nakamura, M. Machida, S. Miyasaka, S. Tajima, and A. Q. R. Baron, **"Magneto-elastic coupling in detwinned $Sr(Fe_{1-x}Co_x)_2As_2$ by inelastic x-ray scattering"**, Oral Presentation (B0.00007)
APS March Meeting 2015, San Antonio, USA

[4] N. Murai, T. Fukuda, T. Kobayashi, M. Nakajima, H. Uchiyama, D.

Ishikawa, S. Tsutsui, H. Nakamura, M. Machida, S. Miyasaka, S. Tajima, and A. Q. R. Baron, **"Magneto-elastic Coupling in Detwinned SrFe$_2$As$_2$by Inelastic X-ray Scattering"**, Oral Presentation (PC-24)
The 27th International Superconductivity Symposium (ISS2014), Tokyo, Japan

[5] N. Murai, T. Fukuda, T. Kobayashi, M. Nakajima, H. Uchiyama, D. Ishikawa, S. Tsutsui, H. Nakamura, M. Machida, S. Miyasaka, S. Tajima, and A. Q. R. Baron, Oral Presentation (9aBD-3)
JPS, September 2014, Chubu University, Japan

[6] N. Murai, T. Masui, M. Ishikado, S. Ishika, H. Eisaki, S. Uchida, S. Tajima, **Superconducting Gap Structure in Out-of-plane-disordered Bi$_2$Sr$_2$CaCu$_2$O$_{8+\delta}$ as Studied by Raman Spectroscopy** Poster presentation (PCP-60)
The 25th International Symposium on Superconductivity (ISS2012), Tokyo, Japan

[7] N. Murai, T. Masui, M. Ishikado, S. Ishika, H. Eisaki, S. Uchida, S. Tajima, Oral Presentation (21aGB-2)
JPS, September 2012, Yokohama National University, Japan

[8] N. Murai, T. Masui, M. Ishikado, S. Ishika, H. Eisaki, S. Uchida, S. Tajima, **Disorder-Induced Change of Gap Anisotropy in Bi$_{2+x}$Sr$_{2-x}$CaCu$_2$O$_{8+\delta}$ Studied by Raman Spectroscopy**, Poster presentation
International Workshop on Heavy FermionsTOKIMEKI 2011, Osaka, Japan

[9] N. Murai, T. Masui, M. Ishikado, S. Ishika, H. Eisaki, S. Uchida, S. Tajima,

Oral Presentation (24pGM-1)

JPS, September 2011, Toyama University, Japan